Journal of Building Engineering 114 (2025) 114177

Contents lists available at ScienceDirect

Journal of Building Engineering

journal homepage: www.elsevier.com/locate/jobe

Mechanical and chemical effects of wet-dry cycling and UV exposure on flax textile reinforced recycled aggregate concrete: role of rice husk ash

Wenzhuo Ma [a], Libo Yan [a,b,*]

[a] Department of Organic and Wood-based Construction Materials, Technische Universität Braunschweig, Hopfengarten 20, 38102 Braunschweig, Germany

[b] Center for Light and Environmentally-Friendly Structures, Fraunhofer Wilhelm-Klauditz-Institut, Riedenkamp 3, 38108 Braunschweig, Germany

ARTICLE INFO

Keywords:
Wet-dry cycling
Ultraviolet (UV) irradiation
Flax fibre
Epoxy
Reinforced recycled aggregate concrete

ABSTRACT

This study examines the effects of wet-dry cycling combined with ultraviolet (UV) irradiation (at 20 °C, 30 weeks) on the mechanical properties and chemical compositions of reinforced recycled aggregate concrete (RAC) reinforced with epoxy-coated flax textile and its individual components, including flax yarn, epoxy, epoxy-coated flax rod, and RAC. One group of reinforced RAC samples incorporated rice husk ash into the concrete, and the influence of rice husk ash on resistance to weathering-induced ageing was also investigated. The mechanical and chemical degradation mechanisms induced by these environmental factors were evaluated by tensile or compression tests and Fourier-transform infrared spectroscopy analysis. The results showed that flax yarns alone underwent severe deterioration, including compound leaching, fibrillation, and discoloration, leading to reduced cellulose and hemicellulose content as well as decreased cellulose crystallinity, along with the formation of chromophoric compounds and microbial activity. The degradation resulted in a significant reduction in tensile loading capacity, with only 7.4 % of residual load capacity remaining. Degradation of epoxy was also observed, with a 20 % reduction in tensile strength due to the breakdown of amide groups and aliphatic structures. In the epoxy-coated flax rod, wet-dry cycling caused flax fibre/epoxy interfacial debonding. Although photo-oxidation of the fibres noticeably reduced the cellulose crystallinity and content, the overall rod showed no significant tensile deterioration, with only a 9 % decrease in average tensile strength and a 10 % decrease in average E-modulus. Both reinforced RAC samples, with or without rice husk ash, retained their tensile properties after exposure, with no significant changes detected in tensile strength, toughness or ultimate strain; however, the flax fibre extracted from the sample without rice husk ash exhibited more severe alkaline degradation in hemicellulose and cellulose crystallinity compared to that from the sample containing rice husk ash. This indicated that incorporating rice husk ash into the RAC helped to mitigate flax fibre degradation and sustain the tensile load capacity of reinforced RAC, due to its pozzolanic reaction which consumed Ca $(OH)_2$, as confirmed by Fourier-transform infrared spectroscopy analysis. In all, this study advances the understanding of the durability of recycled aggregate concrete reinforced with plant-based textiles and proposes an improvement strategy using agricultural waste. The findings

* Corresponding author. Department of Organic and Wood-based Construction Materials, Technische Universität Braunschweig, Hopfengarten 20, 38102 Braunschweig, Germany.

E-mail addresses: l.yan@tu-braunschweig.de, libo.yan@wki.fraunhofer.de (L. Yan).

https://doi.org/10.1016/j.jobe.2025.114177
Received 2 July 2025; Received in revised form 7 September 2025; Accepted 23 September 2025
Available online 24 September 2025

highlight the potential of integrating recycled and bio-based materials to enhance sustainability in construction.

1. Introduction

In recent years, plant-based natural fibres, particularly flax fibre, have attracted increasing attention in the construction and infrastructure industries. Flax fibre has not only achieved a high level of industrialisation in polymer composite applications [1–5] but is also gaining growing interest for use in cementitious composites [6–11]. In addition to being used as randomly oriented discrete fibre reinforcement in cementitious composites, flax fibre has been processed into textile reinforcements, improving fibre reinforcing efficiency [12]. Compared to carbon or alkali-resistant glass fibres, which are traditionally used as textile reinforcements in cementitious composites, flax fibre offers a significantly lower environmental impact. During fibre production, flax fibre contributes to a reduction in greenhouse gas emissions by up to 99 % and 84 %, respectively, when compared to carbon and alkali-resistant glass fibres [13–17]. However, the organic nature of flax fibre makes it prone to degradation not only in aggressive cementitious environment, but also when being exposed to outdoor climate conditions. Saha et al. [18] observed discolouration of sisal and jute fibres after ultraviolet (UV) irradiation, which was primarily attributed to photo-degradation of lignin and the oxidation of cellulose. Furthermore, repeated drying and wetting cycles leads to irreversible stiffening and reduced water absorption capacity of cellulosic fibres, a phenomenon known as hornification [19]. Both UV irradiation and wet-dry cycling can lead to surface erosion of cellulosic fibres [18,20]. Although a polymeric coating is typically applied to flax textiles to protect the fibres from alkaline environment in concrete, it does not fully prevent water permeation into the flax fibre. Additionally, the polymer coating itself, usually epoxy, is susceptible to hydrolysis in an alkaline environment [10] and also vulnerable to photo-oxidation when exposed to UV irradiation [21]. Some researchers have investigated flax fibre reinforced polymer (FFRP) composites under water exposure or wet-dry cycling combined with UV weathering. Their findings indicated that, in addition to the previously mentioned material degradation, debonding between the flax fibre and the polymer also occurred, primarily due to differential wet expansion [20,22].

Once embedded in a concrete, the polymer-coated flax textile (i.e., flax fibre reinforced polymer, hereafter referred to as FFRP) is no longer significantly affected by UV irradiation, as conventional concrete blocks nearly all light from passing through, except in the case of translucent concrete [23]. Instead, the primary challenge for the coated flax textile reinforcement arises from the highly alkaline environment. Certainly, UV irradiation can influence concrete properties, and several researchers have examined its effects on physical and compressive properties of early-age concrete. Wang et al. [24] reported that intense UV exposure after 3 days of curing led to increased drying shrinkage, a reduced degree of hydration, higher carbonation, greater total porosity, and decreased compressive strength in cement mortar. Similarly, Li et al. [25] observed enhanced carbonation in cement-based materials when exposed to UV irradiation after just 1 day of curing. Both studies also highlighted the influence of supplementary cementitious materials, such as fly ash, metakaolin, blast furnace slag, and silica fume, in enhancing UV resistance and increasing carbonation effects [24,25]. However, research on the effects of UV irradiation on the durability of cured concrete (>28 days) remains limited. Prolonged UV exposure could potentially lead to surface discoloration or crack formation, particularly in textile reinforced concrete, which is commonly used for exterior building facades and cladding panels. In addition to UV light, repeated drying and wetting cycles pose a significant challenge to the interface between the concrete and plant-based natural fibre/textile reinforcements. This is not only due to the repeated swelling and shrinkage of plant-based fibres, which can also lead to debonding between the fibre/textile and the concrete, but also because of the enhanced fibre mineralisation [11]. This mineralisation is driven by the reprecipitation of relatively low-strength hydration products, such as secondary ettringite, within the newly formed voids at the former fibre-cement interface [26,27]. Many researchers have investigated the impact of wet-dry cycles on the mechanical properties of cementitious composites reinforced with plant-based natural fibres [28–30], with flexural strength losses ranging from 5 % to 75 %, largely depending on the fibre volume fraction [11]. However, there is still limited understanding of the wet-dry durability of cementitious composites reinforced with textiles made from plant-based natural fibres.

In summary, although plant-based natural fibres, particularly flax fibre, have gained significant attention in cementitious composites, there remains a limited understanding on the long-term durability of flax textile reinforced cementitious composites under challenging environmental conditions. Given the typical applications of textile reinforced concrete, including facades, cladding, roofing systems, custom architectural features, and more, it is crucial to consider the effects of UV irradiation and moisture cycling when investigating the service life of flax textile reinforced cementitious composites. The combined impacts of wet–dry cycling and UV radiation are relevant globally and are particularly pronounced in tropical and subtropical regions. In this study, recycled aggregates ranging from 2 to 8 mm were incorporated into the concrete, as it was observed that the inclusion of medium-sized recycled aggregates (RAs) mitigated debonding of the concrete by enhancing mechanical interlocking with the FFRP grid [9]. Moreover, using recycled aggregates can help reduce the consumption of natural stones, and also alleviate land pressure by reducing the amount of waste sent to landfills. Additionally, rice husk ash (RHA) was incorporated as a supplementary cementitious material in the RAC, as it has been shown to significantly improve the bond properties between FFRP and the RAC [9], while also enhancing the alkaline durability of FFRP in a cementitious environment [10]. Although other supplementary cementitious materials such as metakaolin [31] and silica fume [32] have also been shown to enhance the durability of flax textile reinforced cementitious composites, RHA offers the additional advantages of being a sustainable agricultural by-product and exhibiting high pozzolanic activity (>90 % silica). In this study, the addition of RHA to RAC was expected to enhance the UV resistance of RAC, maintain a strong FFRP/RAC bond under wet-dry cycling, and thereby preserve the load-bearing capacity of flax textile reinforced RAC under weathering exposure. The general objectives of this

work are to (i) understand the material-level degradation mechanisms under combined weathering conditions, and (ii) examine the intrinsic behaviour of the isolated components and their contribution to the overall long-term performance of the reinforced concrete. Specifically, this study aims to:

1) investigate the impact of wet-dry cycling combined with UV irradiation at 20 °C for 30 weeks on FFRP reinforced RAC and their individual components, including flax yarn, epoxy, FFRP rod, and RAC. The research will assess how these environmental factors influence both the mechanical properties and chemical compositions of the materials or composites;
2) improve the weathering durability of the FFRP reinforced RAC by adding RHA to the concrete, aiming to improve the UV resistance of RAC, mitigate moisture-related deterioration at the FFRP/RAC interface and enhance alkaline durability of FFRP in RAC.

2. Experimental program

RAC reinforced with epoxy-coated flax textile along with the constituent components—flax yarn, epoxy, FFRP rod and RAC cylinder—was subjected to simulated weathering ageing, consisting of wet-dry cycling at 20 °C combined with UV irradiation. After 30 weeks of exposure, mechanical tests, including tensile and compression tests, and Fourier-transform infrared (FTIR) spectroscopy analysis, were conducted to assess the effects of ageing on the mechanical properties and chemical composition of all samples.

2.1. Materials

2.1.1. Flax textile

A commercially available flax-based reinforcement mesh (Bcomp® powerRibs™, shown in Fig. 1 (a)) was employed for FFRP production and used in the concrete reinforcement phase of this study. The mesh comprises orthogonally arranged warp and weft yarns, which are secured by an additional binder thread. Each yarn type has a linear mass density of 3000 tex, with an inter-yarn spacing of 28 mm [33]. For the weathering ageing tests, the warp yarns were extracted from the fabric and cut to a length of 400 mm.

2.1.2. Epoxy

The flax fabric was coated using a two-component epoxy system (Gurit® AMPREG™ 31), selected for its favourable mechanical performance, strong adhesion characteristics and low viscosity characteristics. The epoxy formulation is based on a bisphenol-A-epichlorohydrin resin combined with an amine-based curing agent [34]. Following a curing process at 70 °C for 5 h, the epoxy is reported to reach a tensile strength of 78 MPa, a Young's modulus of 3.24 GPa, and a glass transition temperature of 91 °C [35].

2.1.3. Rice husk ash

Rice husk ash (RHA), obtained from a power plant in Lingshou County, China, was used as a supplementary cementitious material. The ash was re-calcined at 600 °C for 3 h and ground at 320 rpm for 30 min using a planetary ball mill. Fig. 2 presents the RHA after pre-treatment. This treatment yielded RHA with a silica content above 90 % (Table 1), a loss on ignition of 2.8 %, and a mean particle size of 9.27 μm. Particle size analysis (Fig. 3 (a)) showed that 50 % of the particles were below 6.48 μm, all under 30 μm. The X-ray diffraction (XRD) pattern (Fig. 3 (b)) confirmed the presence of crystalline silica.

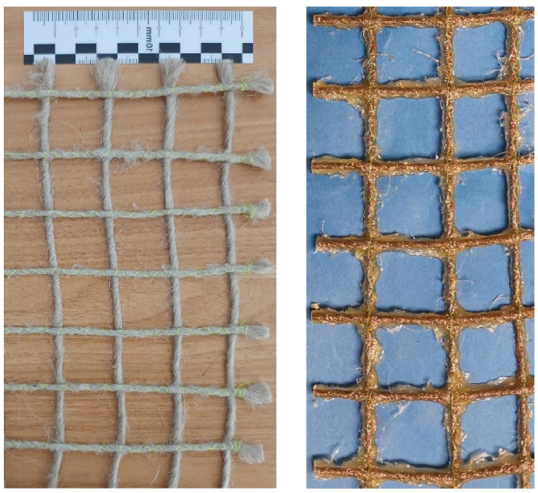

Fig. 1. (a) Flax textile and (b) FFRP.

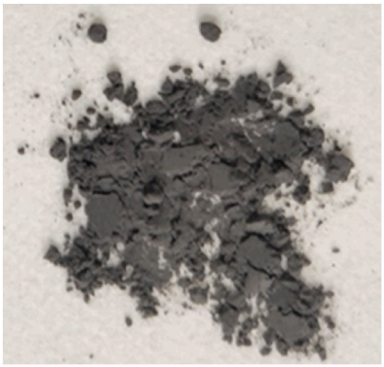

Fig. 2. Rice husk ash after re-burning and grinding [9].

Table 1
Chemical composition of the RHA after pre-treatment [9].

Chemical composition	SiO_2	K_2O	Al_2O_3	CaO	Fe_2O_3	MgO	P_2O_5	Na_2O	SO_3	LOI
%	90.1	3.1	0.6	0.8	0.7	0.5	0.6	0.1	0.2	2.8

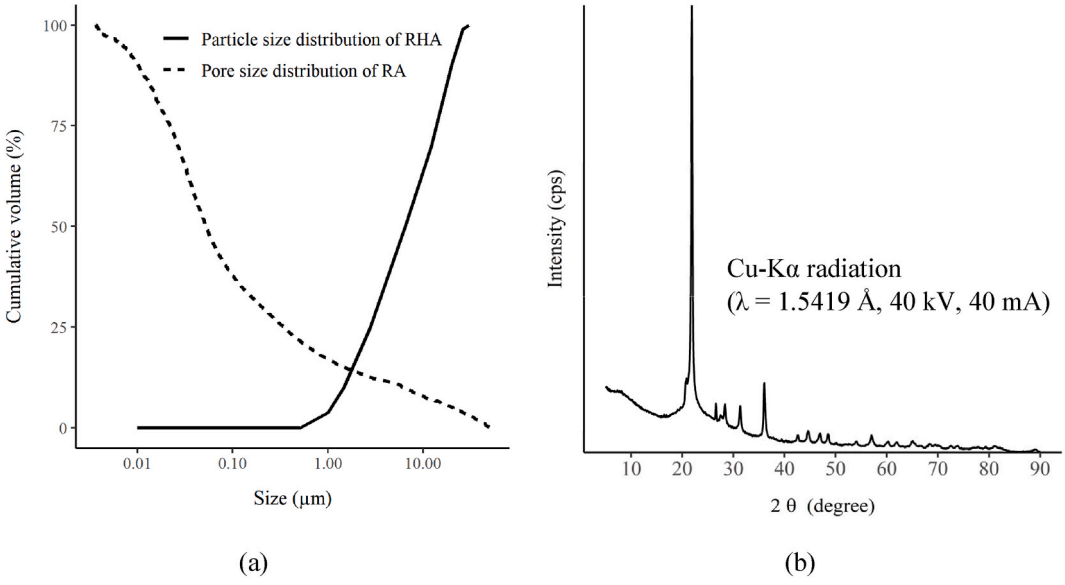

Fig. 3. (a) Particle size distribution of RHA and pore size distribution of RA, (b) the crystalline phase of the RHA from XRD [9].

2.1.4. Recycled aggregate

Recycled concrete aggregates used in this study were sourced from Entsorgungstechnik BAVARIA GmbH (Schwabhausen, Germany, shown in Fig. 4) and sieved to a 2–8 mm size range. The oven-dried density and water absorption were measured as 2662.8 kg/m^3 (±0.1 %) and 4.58 % (±3 %), respectively [9], in accordance with DIN EN 1097-6 [36]. Mercury intrusion porosimetry showed a total pore volume of 29.25 mm^3/g with an average pore radius of 0.05 μm (Fig. 3 (a)). About 52 % of the pores were within 0.01–0.1 μm, and 16 % were between 1 and 100 μm [9]. This fine porosity suggests that RHA may improve RAC performance through its filling effect, as supported by previous findings [37].

2.2. Sample fabrication

2.2.1. Fabrication of FFRP

The flax mesh fabric was stored for more than four weeks under controlled conditions of 20 ± 2 °C and 65 % relative humidity, before FFRP fabrication and the ageing of the yarns. The epoxy was applied using the hand lay-up technique, followed by post-curing at 70 °C for 5 h, 24 h after the coating was applied, as recommended by the technical datasheet [35]. The fabricated FFRP grids (as shown

Fig. 4. Recycled aggregates.

in Fig. 1 (b)) were cut into 400 mm rods for weathering exposure and 500 mm × 100 mm strips for the fabrication of reinforced RAC.

2.2.2. Concrete mixture and casting

The concretes used in this study consisted of RAC and a modified version incorporating RHA as a supplementary cementitious material (RHA*RAC). Both mixtures were prepared in accordance with the mix proportions established in our previous research [9, 10], as detailed in Table 2. In the RHA*RAC, RHA was incorporated as a supplementary cementitious material at a 10 % replacement ratio by weight of the total binder. This proportion was selected based on findings from previous studies [37–40], which identified 10 wt% as the optimal substitution level for cement for enhancing the compressive properties and long-term durability of RAC. Due to the high water absorption of the recycled aggregates (4.58 % [9]), additional water was added to ensure adequate workability of the concrete paste. The required amount was calculated by subtracting the measured moisture content (0.78 %) from the absorption capacity, resulting in 3.8 % extra water relative to the RA weight. A two-stage mixing procedure, as described in Ref. [41], was used to prepare both RAC and RHA*RAC pastes (see Fig. 5). For each 500 mm × 100 mm × 15 mm reinforced panel, a single layer of FFRP reinforcement was embedded at mid-depth, with a reinforcement ratio of approximately 1.2 % along the loading direction. The casting process followed the method previously detailed in our earlier studies [9,10]. After 28 days of curing, the panels were transferred to a weathering chamber. Additionally, Ø100 mm × 200 mm cylindrical specimens were cast using identical mix designs and procedures, and were also placed into the weathering environment.

2.3. Ageing protocol and test methods

Table 3 presents the protocol for the simulated weathering ageing process and the test plan. The cyclic weathering ageing was referred to ASTM G154-16 [42], with each cycle consisting of: 1) 3 h of drying at 20 °C and 65 % relative humidity, 2) 12 h of UV irradiation, 3) another 3 h of drying at 20 °C and 65 % relative humidity and 4) 6 h of rainfall. In the climate chamber, nozzles were installed at each corner to spray tap water, simulating rainfall conditions. UV lamps emitting radiation in the wavelength range of 280–400 nm were mounted on one wall to replicate sunlight exposure. Samples were placed into the chamber in the middle of raining phase and underwent 30 weeks of exposure.

Samples were subjected to tensile or compression tests before and after 30 weeks of exposure. The tensile test on the flax yarn was performed in accordance with DIN EN ISO 2062 [43], using a gauge length of 250 mm and a testing speed of 250 mm/min. Among these, the test on the original flax yarns was conducted at the Application Centre for Wood Fibre Research HOFZET® in Fraunhofer Institute for Wood Research (Fraunhofer WKI) [44]. The tensile test on the FFRP rod was conducted with a gauge length of 150 mm and a testing speed of 2 mm/min, in accordance with ISO 10406-1 [45]. For the dogbone-shaped epoxy sample, the tensile test followed ISO 527-1 [46], using a gauge length of 30 mm and a testing speed of 1 mm/min. FFRP reinforced RAC (FFRP-RAC) and FFRP reinforced RAC containing RHA (FFRP-RHA*RAC) were subjected to uniaxial tensile test, using a gauge length of 340 mm and a displacement speed of 0.5 mm/min, with a reference of RILEM Technical Committee 232-TDT [47]. Additionally, the RAC and RHA*RAC cylinders were also tested under compression load. Their compressive strength and E-modulus were measured according to DIN EN 12390-13 [48], using a loading speed of 0.5 MPa/s.

Table 2
Mix proportions for different concretes (by weight) [9].

Concrete	Cement	RHA	Water	Sand (0.08–2 mm)	RA (2–8 mm)	Superplasticiser	Additional water
RAC	1	–	0.4	0.97	0.49	0.015	0.019
RHA*RAC	0.9	0.1	0.4	0.97	0.49	0.015	0.019

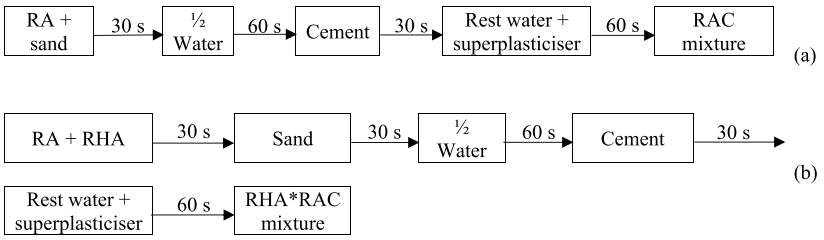

Fig. 5. Mixing procedures for (a) RAC and (b) RHA*RAC [9].

Table 3
Ageing protocol and test matrix.

Sample	Ageing protocol	Replication	Mechanical test
Flax yarn	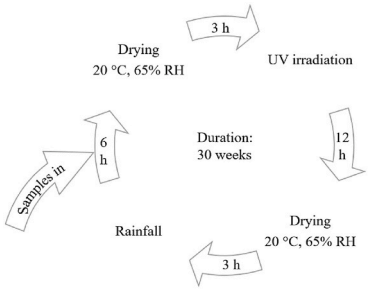	10	Tensile test before/after exposure
Epoxy		10	
FFRP rod		10	
RAC cylinder		3	Compression test before/after exposure
RHA*RAC cylinder		3	
FFRP-RAC		5	Tensile test before/after exposure
FFRP-RHA*RAC		5	

FTIR was employed to analyse changes in the chemical composition of samples resulting from weathering exposure. Flax fibres were extracted from five sources: the original yarn, exposed yarn, exposed FFRP, exposed FFRP-RAC, and exposed FFRP-RHA*RAC. Measurements were conducted with five replications for each condition, except for the original yarn, which was measured using three replications. Samples were also taken from the surface of both the original and exposed epoxy, with three and five replications, respectively. Additionally, concrete debris from the compressed samples was collected from regions located 0–20 mm beneath the concrete surface. The mortar portion was ground using a pestle and then sieved to obtain cementitious powder with particle sizes below 50 μm (excluding sand particles). This powder was used for FTIR measurements, conducted with five replications. All measurements were performed using 32 scans at a resolution of 4 cm^{-1}, covering a wavenumber range from 400 to 4000 cm^{-1}.

3. Results and discussion

3.1. Flax yarn

3.1.1. Changes in morphology and weight

The flax yarn subjected to the weathering condition exhibited various morphological changes. Fig. 6 (a) provides an overview of the exposed flax yarn, while the typical morphological alterations observed under an optical microscope are shown in Fig. 6(b)–(d). Discolouration is one of the most visible consequences of exposing lignocellulosic fibres to UV irradiation, primarily driven by the photo-degradation of lignin and the oxidation and hydrolysis of cellulose [18]. Fig. 6 (b) shows the discolouration of the flax yarn after 30-week exposure, showcasing a significant transformation compared to the original yarn. The flax fibres exhibited whitening and transparent as a result of the prolonged combined effects of UV irradiation and wet-dry cycles. The wet-dry cycling likely exacerbated the discoloration phenomena. Repeated swelling and shrinking exposed internal lignin and cellulose to UV light, accelerating both photo-degradation and photo-oxidation. The degradation of lignin and pigments produced water-soluble compounds, which were readily leached out during water spraying, further enhancing the whitening effect. Additionally, these processes may have induced changes in the fibre structure, such as increasing fibre crystallinity. This structural reorganisation likely contributed to the observed transparency of the flax fibres. Fig. 6 (c) illustrates a rougher surface of the flax yarn after exposure. Both UV irradiation and wet-dry cycling can contribute to surface erosion of lignocellulosic fibres [18,20]. This process weakens the fibre's structural integrity, leading to the microcracking and the splitting of microfibrils. Over time, these structural changes manifest as fibre fibrillation, where individual fibrils detach from the main fibre, creating a rougher surface and further compromising the mechanical properties. Fig. 6 (d) showed the fibre fibrillation along with the darkened appearance of the yarn's surface. During the UV irradiation, lignocellulosic fibres undergo different various degrees of discolouration, with darkening and yellowing being the most common effects. These colour changes are primarily due to the formation and accumulation of chromophoric compounds resulting from the degradation of lignin. In the case of Fig. 6 (d), the chromophores produced during UV exposure adhered to the fibre surface. Despite the wet-dry cycling, these

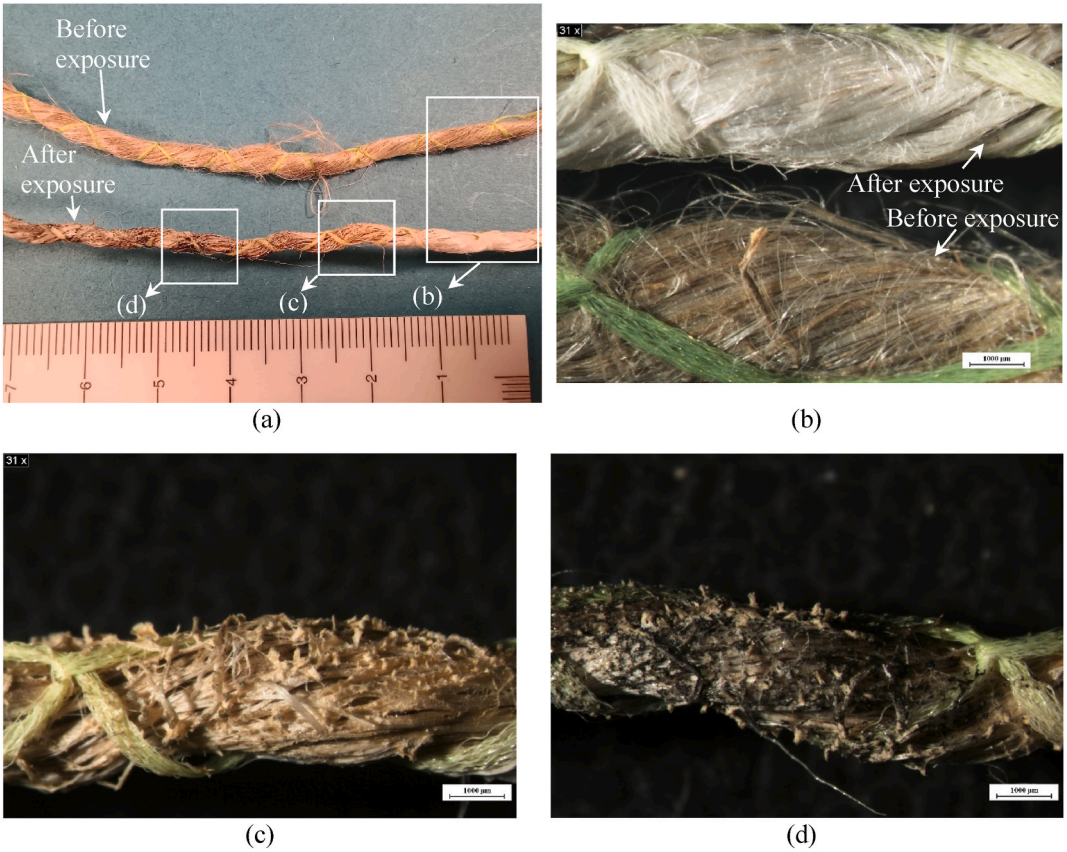

Fig. 6. (a) Comparison of the overall morphology of flax yarns before and after exposure, (b) discolouration of the exposed flax yarn compared with the yarn before exposure, (c) fibre fibrillation and (d) fibre fibrillation along with surface darkening observed on the exposed flax yarn.

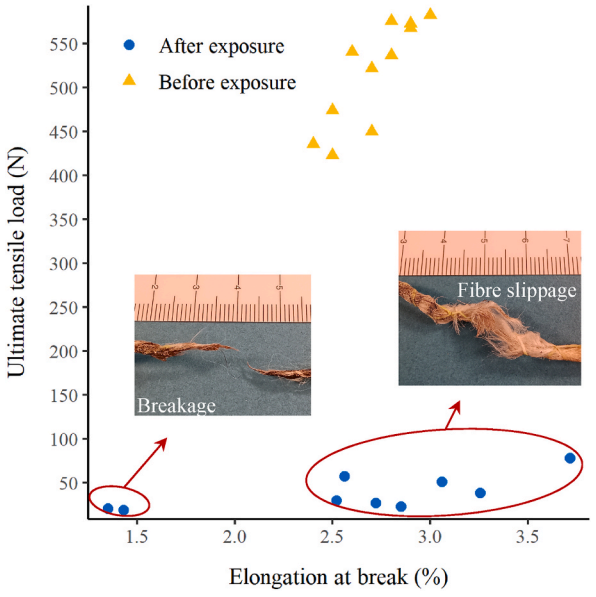

Fig. 7. Tensile properties of flax yarns before and after exposure.

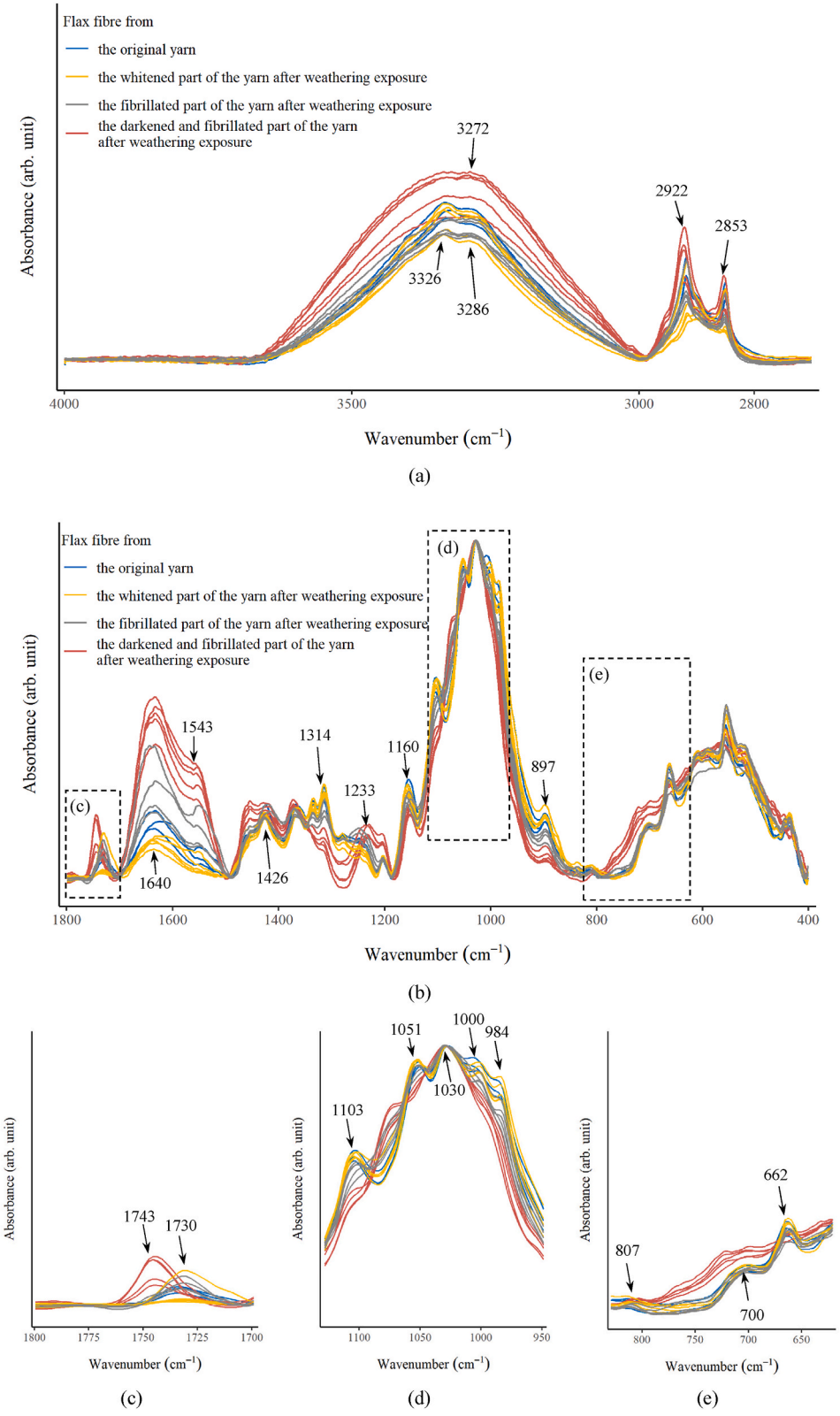

Fig. 8. Normalised FTIR spectra of flax fibres from the yarn before and after exposure: (a) 4000–2700 cm^{-1}, (b) 1800–400 cm^{-1}, (c) 1800–1700 cm^{-1}, (d) 1130–950 cm^{-1} and (e) 830–620 cm^{-1}.

compounds did not leach out, resulting in a darkened surface of the flax yarn. In addition, the flax yarn suffered from fibre fibrillation also showed an increased brittleness and hardness, which can be observed as a lack of flexibility during yarn bending.

The weight of the flax yarns was measured both before and one week after weathering exposure. Outside the exposure period, the yarns were stored in a climate room at a temperature of 20 ± 2 °C and a relative humidity of 60 ± 5 %. The weight loss compared to the original weight of flax yarn ranged from 0.07 % to 0.57 %. This mild weight loss is attributed to the oxidative and photochemical breakdown, with the leaching out of degraded by-products as previously mentioned. The degradation at certain parts of the yarn is likely confined to the surface level, resulting in a typically small weight loss.

3.1.2. Changes in tensile properties

The flax yarn experienced substantial reduction in tensile load capacity after weathering exposure, which is evident in Fig. 7. The average ultimate tensile load of the exposed yarns is only 7.4 % of the original average value. Fig. 7 shows the corresponding failure modes. Only two of the exposed yarns failed in breakage under tensile load, whereas the majority failed due to fibre slippage. The two samples that failed due to breakage both fractured at the blackened sections of the yarns, where fibre fibrillation was also observed. These two broken yarns exhibited remarkably decreased elongation, indicating the increased brittleness at these sections of the yarn, as mentioned in Section 3.1.1. This brittleness primarily resulted from lignin degradation and fibre fibrillation. Moreover, the splitting of microfibrils caused fibrillation. This process compromised the mechanical integrity of the yarn and resulted in a significant reduction in strength. Yarn untwisting and the subsequent fibre slippage occurred more frequently when the exposed yarns were subjected to tensile stress. It was visible that, at certain positions along the yarn, particularly in areas with whitening discoloration but no fibre fibrillation, the external fibres aligned nearly parallel prior to tensile testing. The absence of cohesion forces among the fibres rendered them prone to slippage under tensile stress. The measured yarn elongation reflected the slip displacement occurring between fibres, resulting in elongation values higher than those of the broken yarns. The yarn untwisting was mainly attributed to the wet-dry cycling, during which the repetitive swelling gradually relaxed the internal stresses within the yarn, destabilising the twisted configuration and promoting untwisting. This can also be verified by the fact that untwisting typically happened in regions where leaching was concentrated. The varied failure modes of the exposed yarns resulted in more scattered elongation measurements and also increased the coefficient of variation of the ultimate tensile load to 4.5 times its original value. The load-bearing capacity of exposed yarns that failed by breakage was generally lower than that of yarns that failed due to fibre slippage. This can be attributed to the fact that fracture consistently occurred in the blackened regions of the yarns, where extensive photo-degradation and fibrillation were observed. As evidenced by the FTIR analysis presented in Section 3.1.3, these regions exhibited a significant reduction in both cellulose content and crystallinity. Consequently, the tensile strength of the flax fibres in these areas was markedly diminished, falling below the frictional resistance required for fibre slippage. Furthermore, among yarns that failed via slippage, the degree of untwisting varied considerably. This led to a heterogeneous distribution of cohesive and frictional forces among the constituent fibres, manifesting as a broad dispersion in ultimate tensile load values. To summarise, the primary impact of wet-dry-UV irradiation cyclic exposure on the mechanical structure of flax yarn were untwisting, increased brittleness, and, as a result, a significant reduction in tensile strength.

3.1.3. Changes in chemical composition

Flax fibres extracted from various sections of the exposed yarn, as shown in Fig. 6, were analysed using Fourier-transform infrared (FTIR) spectroscopy. Their spectra were then compared with those of fibres from the original, unexposed yarn. To eliminate the intensity variations caused by factors such as sample thickness, sample concentration and path length during measurements, all spectra were normalised to ensure that the analysis focuses on relative differences in the chemical composition or structural changes. The normalisation was conducted based on the absorbance at 1030 cm^{-1}, with its intensity set to 1 [49–52]. The normalised FTIR spectra

Table 4
Assignments and correlated compounds in the FTIR spectra for flax fibre.

Wavenumber (cm^{-1})	Assignment	Correlated compounds	Reference
3700–3000	ν(O-H)	Cellulose	[53,54]
~2922	ν(C-H)	Polysaccharides	[57,58]
~2853	ν(CH_2)	Wax	[54,58]
~1730	ν(C=O) ester bond	Hemicellulose	[50,53,57,59]
~1640	δ(O-H)	Absorbed water	[55,56]
~1543	δ(N-H) amide II	Proteins or amino acids	[55,60,61]
~1426	δ(CH_2)	Cellulose, designated as a “crystalline” absorption band	[55,62]
~1314	ρ(CH_2)	Cellulose	[55,56]
~1233	ν(C=O) or NH_2 deformation	Pectic substances or amino acids	[55,63]
~1160	ν(C-O-C)	Cellulose	[55,64,65]
~1103	ν(C-O-C) glycosidic bond	Cellulose	[57–59]
~1051	ν(C-OH)	Cellulose	[57,59]
950–1000	ν(C-O-C) glycosidic bond and ν(C=C) aromatic ring	Polysaccharides	[55,59]
~897	ν(C-O-C) β-glycosidic linkage	Cellulose	[49,55]
~807	ν(C=C) aromatic ring, in-plane	Hemicellulose	[58,59]
~700	ρ(CH_2)	Crystalline cellulose	[55,66]
~662	δ(O-H) ring structure, out of plane	Indicator of cellulose	[55,67,68]

(ν: stretching, δ: scissoring and ρ: rocking).

are presented in Fig. 8, with the key vibrational bands and their corresponding assignments provided in Table 4. To quantitatively investigate the differences in chemical composition among the groups, the integrated intensity (I) of the correlated vibration bands was determined by calculating the area under a specific band within a defined range of wavenumbers. Table 5 lists the values for all the groups.

Fig. 8 (a) shows the spectra in the region of 4000–2700 cm^{-1}. The vibrational bands in the region of 3700–3000 cm^{-1} are typically assigned to the stretching vibrations of hydrogen bonding in cellulose [53,54]. It is evident in Fig. 8 (a) that the flax fibres from all groups, except for the darkened section of the exposed yarn, exhibit two peaks at 3326 and 3286 cm^{-1}. These peaks correspond to intra-molecular and inter-molecular hydrogen bonding of cellulose, respectively [55]. In contrast, the spectra of the flax fibre sampled from the darkened section of the exposed yarn show a broader band with increased intensity in the region of 3700–3000 cm^{-1}. Tukey's HSD test reveals that the integrated intensity in this region for the fibre from the darkened section of the exposed yarn is significantly greater than that of fibres from other sections, with all adjusted p-values being <0.001 (as shown in Table 5). This suggests a higher degree of hydrogen bonding in the darkened fibre, since hornification stimulates strong interfacial cross-linkages between the cellulose fibrils by hydrogen bonds. The vibration at 1640 cm^{-1} is also associated with hydroxyl groups; however, in this case, it originates from absorbed water [55,56]. The fibrillated fibres exhibit a higher integrated intensity at this wavelength, as the scattered fibrils are more prone to moisture absorption. In contrast, the whitened fibre exhibited reduced intensity at 1640 cm^{-1}. This could be attributed to hornification occurring in this section, which reduced the lumen diameter and decreased its hydrophilic nature, though the change was not considerable. Distinct variations are also evident in the peaks at 2922 and 2853 cm^{-1}, which are typically associated with polysaccharides and wax, respectively [54,57,58]. It can be observed that most of the whitened fibres show little to no peaks in the 3000–2800 cm^{-1} region, indicating degradation and leaching of the compounds as further discussed in Section 3.1.1. The darkened fibre exhibits significantly higher integrated intensity at the peaks of 2922 and 2853 cm^{-1} compared to the whitened fibre and the fibre subjected only to fibrillation (both adjusted p-values <0.05), but shows no significant difference when compared to the original fibre. This suggests that the darkened fibre could still retain its polysaccharides and wax content.

To clearly present the spectra of different groups in Fig. 8 (b), certain unclear regions are zoomed in and illustrated in Fig. 8(c)–(e). Fig. 8 (c) shows the peak at 1730 cm^{-1}, which is assigned to ester bond stretching in hemicellulose [50,53,57,59]. It is evident that the peak shifted to 1743 cm^{-1} for the darkened fibre, suggesting the formation of new carbonyl groups, which act as chromophoric groups resulting from the photolysis of lignin. Additionally, the whitened fibre shows significantly decreased integrated intensity at 1730 cm^{-1} compared to the darkened fibre and the fibre subjected only to fibrillation (both adjusted p-values <0.05). This reflects the possible degradation of hemicellulose that occurred in the whitened part of the yarn. Moreover, the spectra of the different fibre groups exhibit distinct patterns at 1543 cm^{-1}. The fibres underwent fibrillation show noticeable peaks at 1543 cm^{-1}, whereas most of the original and whitened fibres do not exhibit peaks at this wavenumber. The vibration at 1543 cm^{-1} is assigned to amide II, which is attributed to proteins or amino acids [55,60,61]. Based on this, it is presumed that microbial activity, such as mould growth, occurred on the yarn that underwent fibrillation. The fibrillation process may have made the yarn surface more susceptible to microbial colonisation by increasing surface area or by creating conditions (e.g., moisture retention) conducive to microbial growth. However, this finding should be further confirmed through microbiological tests, such as direct optical microscopy, swabbing samples from the yarn followed by culturing on selective fungal growth media for visual identification, or even by measuring enzymes produced by fungi. In the region of 1500–1180 cm^{-1}, the darkened fibre exhibits a spectral pattern that is markedly different from that of the other fibre samples. Most notably, the spectra of the darkened fibre show attenuated peaks at 1426 and 1314 cm^{-1} compared to other fibre samples. Both of these vibrations are associated with cellulose, with the vibration at 1426 cm^{-1} serving as an indicator of cellulose crystallinity [55,56,62]. The discrepancies at these two peaks indicate that more intense cellulose degradation occurred in the darkened fibre. Furthermore, the darkened fibre shows a distinct peak at 1233 cm^{-1}, attributing to pectic substances or amino acids

Table 5
Integrated intensity of the vibrations located at various wavenumbers for flax fibres sampled from different yarn sections (coefficients of variation are indicated in brackets. The same superscript letter indicates a significant difference at the $\alpha = 0.05$ level for the corresponding properties between the two groups, with the adjusted p-values shown in the last row.).

Fibre sampling location	$I_{3326+3286}$ (3700–3000 cm^{-1})	$I_{2922+2853}$ (3000–2800 cm^{-1})	I_{1730} (1775–1700 cm^{-1})	I_{1640} (1700–1580 cm^{-1})	I_{1543} (1580–1500 cm^{-1})	I_{1160} (1140–1185 cm^{-1})	I_{897} (910–840 cm^{-1})
The original yarn	133.4 (±5 %)^{a}	19.1 (±17 %)	1.4 (±31 %)^{f}	16.7 (±29 %)^{j}	4.4 (±50 %)^{n}	7.6 (±2 %)^{r,s}	5.9 (±5 %)^{v,w}
The whitened part on exposed yarn	122.4 (±10 %)^{b}	13.9 (±29 %)^{d}	0.3 (±43 %)^{g,h}	9.3 (±18 %)^{k,l}	1.8 (±66 %)^{o,p}	7.2 (±3 %)^{t}	6.5 (±16 %)^{x,y}
The fibrillated part on exposed yarn	129.8 (±9 %)^{c}	15.4 (±16 %)^{e}	1.5 (±22 %)^{g,i}	26.9 (±27 %)^{l,m}	8.8 (±38 %)^{p,q}	6.7 (±5 %)^{u,s}	3.5 (±17 %)^{w,y}
The darkened and fibrillated part on exposed yarn	190.6 (±12 %)^{a,b,c}	22.2 (±18 %)^{d,e}	3.0 (±34 %)^{f,h,i}	39.6 (±11 %)^{j,k,m}	15.9 (±14 %)^{n,o,q}	5.0 (±10 %)^{r,t,u}	2.3 (±30 %)^{v,x}
adj. p per Tukey's HSD test	a:0.0007 b < 0.0001 c < 0.0001	d:0.0122 e:0.0424	f = 0.0153 g = 0.0402 h < 0.0001 i = 0.0122	j = 0.0001 k < 0.0001 l = 0.0004 m = 0.0065	n < 0.0001 o < 0.0001 p = 0.0019 q = 0.0019	r < 0.0001 s = 0.0116 t < 0.0001 u < 0.0001	v < 0.0001 w = 0.0040 x < 0.0001 y < 0.0001

($I_{3326+3286}$ (3700–3000 cm^{-1}): integrated intensity of the vibrations located at 3326 cm^{-1} and 3286 cm^{-1}, calculated between 3700 and 3000 cm^{-1}).

[55,63]. Considering the other fibre samples show no obvious peaks at this wavenumber, the vibration is more likely attributed to amino acids. This aligns with the observation at 1543 cm^{-1}, suggesting that mould growth may have occurred on the fibrillated yarn.

The vibrational bands in the region of 1180–650 cm^{-1} are primarily associated with polysaccharides, with most vibrations providing information about cellulose. First, the peak at 1160 cm^{-1} is typically assigned to the asymmetric C–O–C stretching in cellulose [55,64,65]. Tukey's HSD test indicates that both fibrillated fibres (with or without darkened discoloration) exhibit a significantly decreased integrated intensity at 1160 cm^{-1} compared to the original fibre, with both adjusted p-values <0.05. Furthermore, the darkened fibre displays a significantly lower integrated intensity at this wavenumber than the whitened fibre (adjusted p-value <0.0001). Additionally, Fig. 8 (d) presents the spectra in the region of 1130–950 cm^{-1}, showing varying peak distributions among the fibre samples. It is clearly evident that, compared to the other samples, the darkened fibre shows absent bands at 1103, 1051, 1000, and 984 cm^{-1}. Among these vibrations, the bands at 1103 and 1051 cm^{-1} are attributed to cellulose [57–59], while the precise assignment of the bands at 1000 and 984 cm^{-1} is challenging due to the coupled nature of the vibrations [55,59]. The fibre subjected only to fibrillation also shows weakened peaks at these wavenumbers; however, the peaks remain faintly visible. Similarly, the peak at 897 cm^{-1} is also characteristic of cellulose, assigned to the stretching of β-glycosidic linkage [49,55]. Both fibrillated fibres, whether with or without darkened discoloration, show a significantly reduced integrated intensity at 897 cm^{-1} compared to the original fibre and the whitened fibre (all adjusted p-values <0.01). Moreover, in the region of 830–620 cm^{-1} as shown in Fig. 8 (e), the darkened fibre also exhibits disappeared bands at 807, 700 and 662 cm^{-1}, which represent hemicellulose, cellulose and cellulose indicator, respectively [55,58,59,66–68]. All observations in the region of 1180–650 cm^{-1} indicate significant cellulose degradation in the fibrillated fibres, with the darkened fibre exhibiting more pronounced degradation.

In summary, the fibre sampled from the whitened portion of the flax yarn exhibited decreased moisture absorption ability, along with reduced hemicellulose and waxy substances; however, these changes were not significant compared to the original fibre. The fibres sampled from the fibrillated part of the flax yarn showed reduced cellulose content and signs of mould growth. Among the fibrillated fibres, the fibre suffered from both fibrillation and darkened discolouration experienced more pronounced cellulose degradation and microbial activity. The darkened fibre also showed decreased cellulose crystallinity, increased moisture absorption ability, and formation of chromophoric groups due to the photolysis of lignin.

3.2. Epoxy

3.2.1. Changes in morphology and chemical composition

Fig. 9 shows the yellowing of epoxy after the exposure, which is typically due to UV-induced photo-degradation. The photo-oxidation primarily affects the bisphenol A-derived structures and the aliphatic portions of the epoxy network. This process leads to the formation of carbonyl groups, which are common chromophores and play a key role in the characteristic yellowing observed after prolonged UV exposure [21].

Fig. 10 presents the FTIR spectra of the epoxy samples before and after exposure. The spectra were normalised to the intensity of the band at 1606 cm^{-1}, assigned to C=C stretching in aromatic rings, which remains relatively stable under UV exposure [22,69]. The assignments of the corresponding vibrations are provided in Table 6, and the integrated intensities of these vibrations were also calculated. The *t*-test revealed significant reductions in the integrated intensity of the exposed epoxy at 3376, 3000–2750, 1742, and 1655 cm^{-1}, compared to the original epoxy (all adjusted p-values <0.05), as highlighted in red in Table 6. It suggests that weathering exposure, primarily UV irradiation, caused significant degradation of the amine groups/hydrogen bonds as well as the aliphatic portions, aldehyde and amide groups in the cured epoxy. Among these, the aldehyde group, present in the original epoxy samples and identified at 1742 cm^{-1}, originates from the formaldehyde included in the Ampreg 31 resin mixture [34]. Formaldehyde undergoes degradation when exposed to UV irradiation and is ultimately oxidised into H_2O and carbon dioxide CO_2 [70–72]. Amin et al. [73] reported that the photolysis process achieved approximately 46 % efficiency in the removal of formaldehyde within 60 min. The photolysis degradation of formaldehyde led to nearly zero integrated intensity of the band at 1742 cm^{-1} for the epoxy sample after exposure. Additionally, the significant reduction in the integrated intensity in the 3000–2750 cm^{-1} region supports the previous statement that photo-oxidation primarily targets the aliphatic portions of the epoxy network. Indeed, the decrease of the integrated intensity at 760 cm^{-1} is also significant at the $\alpha = 0.1$ level (adjusted p-value = 0.0824). This band attributes to the C-H out-of-plane

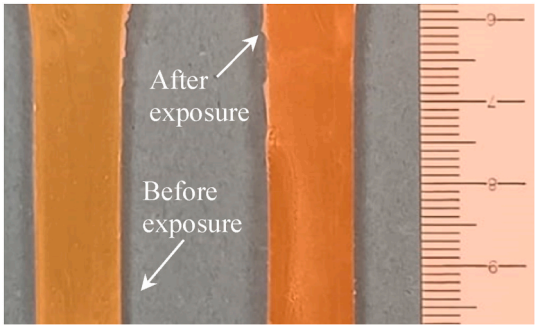

Fig. 9. Yellowing of epoxy after weathering exposure.

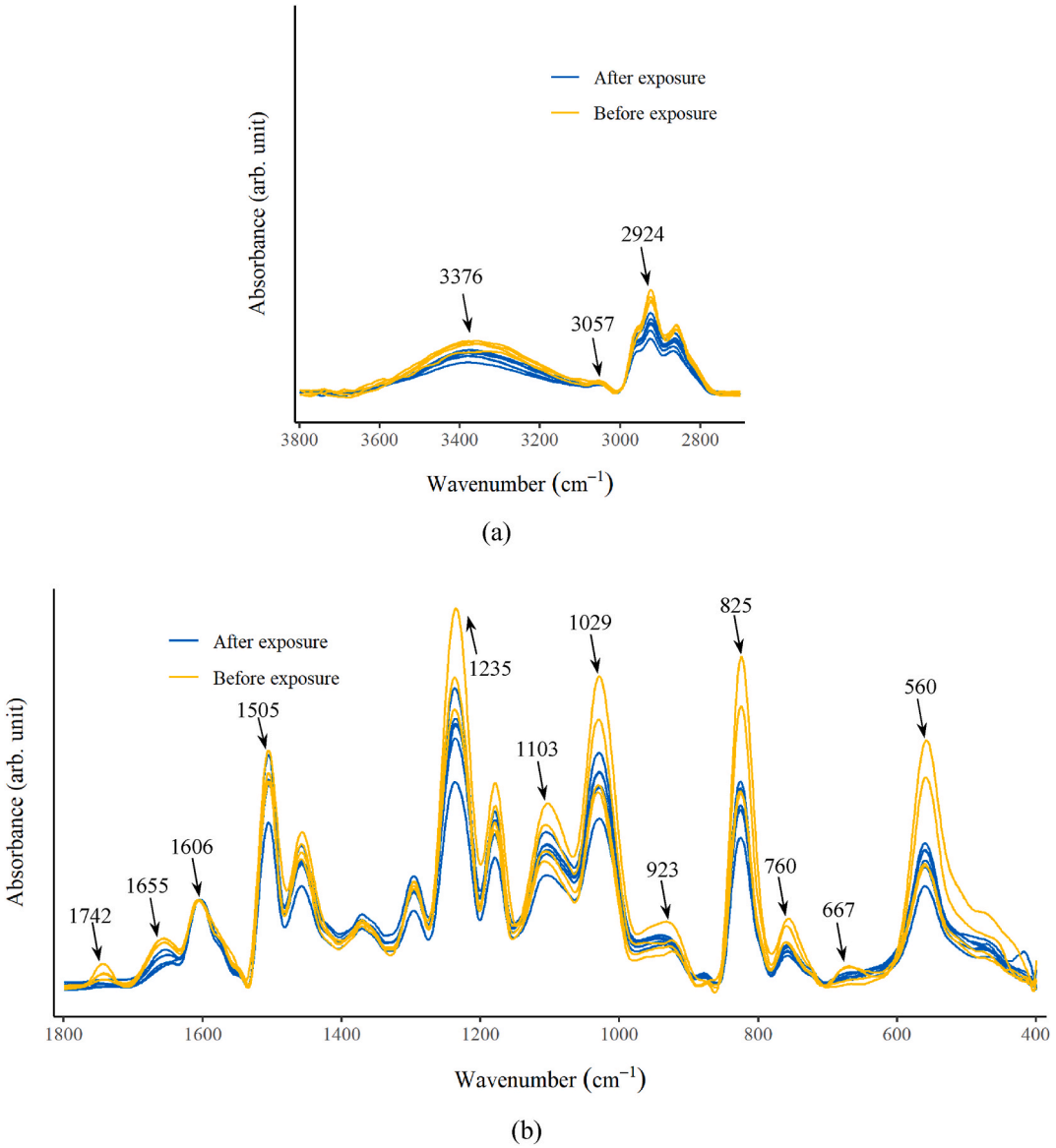

Fig. 10. Normalised FTIR spectra of the epoxy samples before and after exposure: (a) 3800–2700 cm^{-1} and (b) 1800–400 cm^{-1}.

bending of aromatic ring [74–76], indicating that the photo-oxidation also had a notable effect on the bisphenol A-derived structures. The photo-oxidation product carbonyl groups are common chromophores leading to yellowing of epoxy after UV irradiation, typically showing the vibration at 1730–1750 cm^{-1} [69,77]. However, no evident peak is observed in this carbonyl region of the spectra for the exposed epoxy in Fig. 10 (b). This absence could be attributed to the limited formation of chromophores, as there was minimal discoloration observed, as shown in Fig. 9. Moreover, the vibration at 1655 cm^{-1} corresponds to the amide groups [74,78,79], which are the crosslinks formed by amine group from the hardener with oxirane group from the resin (this reaction may also involve formaldehyde). The significant reduction in integrated intensity at 1655 cm^{-1} suggests the breakdown of amide groups, compromising the epoxy network, leading to decreased mechanical properties. In terms of changes in other chemical groups, ether and oxirane groups also exhibit a tendency to degrade. However, the decrease in the integrated intensity of their associated vibrations is not statistically significant.

3.2.2. Changes in tensile properties

As a result of the cross-link degradation described in Section 3.2.1, the epoxy generally showed a reduction in tensile strength and elasticity following UV irradiation. Fig. 11 illustrates the tensile strength and E-modulus of the epoxy, comparing the values measured before and after exposure. As analysed using Student's t-test, the tensile strength decreased significantly after exposure (p-value = 0.0015), with a 20 % reduction in the average value. No significant change in the E-modulus was observed according to the *t*-test (p-

Table 6
Assignments in the FTIR spectra for epoxy.

Wavenumber (cm^{-1})	Assignment	Reference
3500–3200	ν(N-H) (amine group) and ν(O-H)	[79–82]
~3057	ν(C-H) (oxirane ring)	[82–84]
3000–2750	ν(C-H) (alkanes)	[74,82]
~1742	ν(C=O) (aldehyde)	[74,77,82,85]
~1655	ν(C=O) (amide)	[74,78,79]
~1606	ν(C=C) (aromatic ring)	[81–84]
~1505	ν(C=C) (aromatic ring)	[79,81,83–85]
~1235	ν(C-O-C) (aromatic ether)	[78,79,81]
~1103	ν(C-O-C) (ether group)	[80,85]
~1029	ν(C-O-C) (ether group)	[79,80,84]
~923	ν(C-O-C) (oxirane group)	[80,82,84,86]
~825	ν(C-O-C) (oxirane group)	[80,84,87]
780–620	δ(C-H) (aromatics, out-of-plane)	[74–76]
~560	ν(C-Cl) (chloromethyl)	[74]

(ν: stretching and δ: scissoring; the vibrations at the wavenumbers highlighted in red show significant differences in integrated intensity between the epoxy before and after exposure, as determined by a *t*-test at the α = 0.05 significance level.).

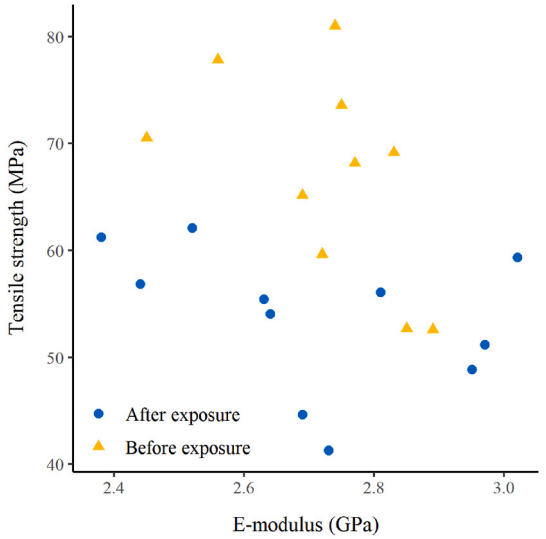

Fig. 11. Tensile properties of epoxy before and after exposure.

value = 0.8852), although a slight increase in the average value (by 0.4 %) was noted. The decreased tensile strength can be explained by the chain scission of aliphatic portions and degradation of amide crosslinks within the epoxy network discussed in Section 3.2.1. These changes in chemical groups led to a reduced crosslink density, weakening the structural integrity of the epoxy and consequently diminishing its ability to bear tensile loads.

3.3. FFRP

3.3.1. Changes in morphology

One FFRP sample was found to be fractured upon removal from the weathering chamber, as presented in Fig. 12. The fracture occurred on the external epoxy coating, accompanied by delamination between the epoxy coating and the flax fibre bundles. These issues primarily resulted from the differing hygroscopic properties and the corresponding mismatch in expansion coefficients between flax yarn and epoxy. The repeated absorption and evaporation of moisture created stress at the interface between the epoxy coating and the flax yarn. Over time, this cyclic stress caused delamination at the interface and fractures in the epoxy coating. The fracture of epoxy coating exposed flax fibres to the weathering condition. The exposed internal fibres exhibited similar discoloration phenomena as outlined in Section 3.1.1, with some fibres displaying whitening and others darkening. In contrast, the fibres that were not exposed to the environment, where the FFRP retained its integrity, maintained their original morphology.

As the reinforcement within RAC, epoxy coating fracture and debonding at the flax/epoxy interface may potentially compromise the long-term structural performance of the reinforced RAC. This degradation of interface integrity can reduce the efficiency of stress

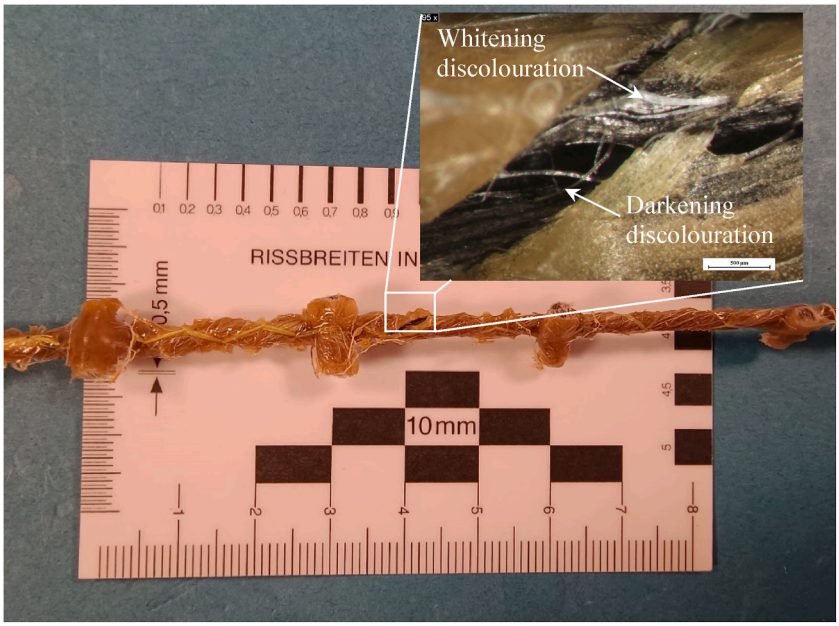

Fig. 12. Fractured FFRP after weathering exposure.

transfer between the fibres and the epoxy matrix, leading to a decrease in overall load-bearing capacity and durability over time, particularly under cyclic loading. Moreover, moisture ingress will exacerbate interface weakening, not only between the fibre and epoxy but also between the FFRP and RAC matrix. This can further accelerate alkaline hydrolysis and mineralisation of flax fibres. To better understand these effects, further long-term durability studies simulating realistic environmental conditions, including repeated loading, are needed. Such investigations would provide valuable insights into the lifespan and reliability of reinforced RAC in practical applications and help develop strategies to improve interface stability and overall composite performance.

3.3.2. Changes in tensile properties and chemical composition of flax fibre

The FFRP samples that retained their integrity after weathering exposure were subjected to tensile testing. Fig. 13 illustrates a comparison of tensile properties between the exposed and unexposed samples. Although the exposed FFRP rods exhibited a 9 % decrease in average tensile strength and a 10 % decrease in average E-modulus compared to the unexposed rods, both reductions were not statistically significant according to the *t*-test (p-values = 0.2558 and 0.1367, respectively).

Fig. 14 presents the normalised FTIR spectra of flax fibres extracted from both exposed FFRP and unexposed yarn, highlighting

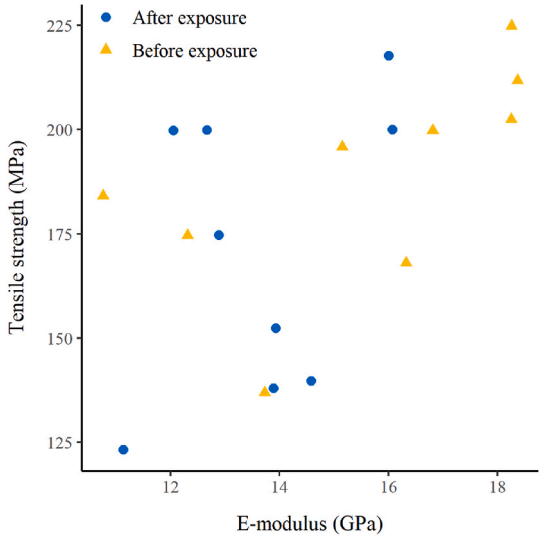

Fig. 13. Tensile properties of FFRP before and after exposure.

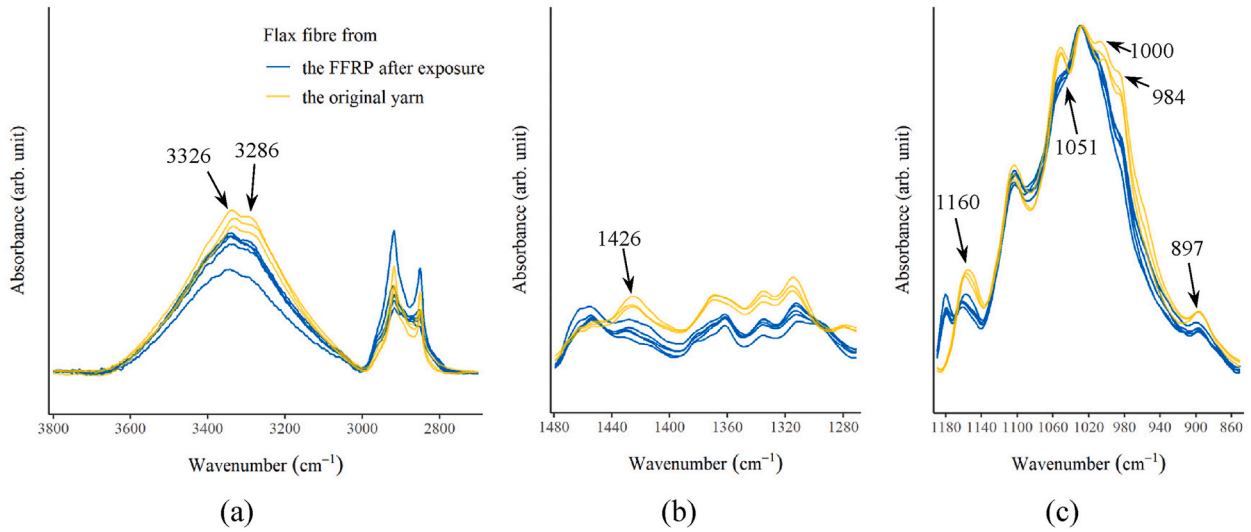

Fig. 14. Normalised FTIR spectra of flax fibre from the exposed FFRP compared to the original fibre: (a) 3800–2700 cm^{-1}, (b) 1480–1280 cm^{-1} and (c) 1190–850 cm^{-1}.

regions with evident spectral changes. Significant differences in integrated intensity were observed at 3700–3000 cm^{-1}, 1426 cm^{-1}, 1160 cm^{-1}, and 897 cm^{-1}, with corresponding p-values of 0.0411, 0.0015, 0.0001, and 0.0003, respectively, as determined by the *t*-test. According to the assignments summarised in Table 4, all of these vibrations are associated with cellulose. Additionally, t-tests were not conducted on the bands at 1051, 1000 and 984 cm^{-1}, as the vibrations at these wavenumbers in the FTIR spectra of the flax fibre extracted from FFRP were visibly diminished. Furthermore, although the bands at 2922 and 2853 cm^{-1} for the fibre from exposed FFRP tended to fade (with the exception of one sample showing particularly sharp bands), the integrated intensity did not show a statistically significant decrease compared to that for the fibre before exposure. Due to epoxy residues on the fibre extracted from FFRP, additional bands were observed. One such band, around 1180 cm^{-1}, is assigned to C–O stretching on the aromatic ring [76]. These epoxy residues also contribute to some inconclusive spectral changes. For instance, some fibres extracted from exposed FFRP exhibited a notable decrease in integrated intensity around 1740 cm^{-1} compared to the original fibre, which could be linked to the degradation of hemicellulose or possibly the breakdown of aldehyde in epoxy. Meanwhile, other samples showed a visible increase in integrated intensity, potentially due to the presence of undegraded aldehyde in the epoxy.

Overall, cellulose degradation occurred in the flax fibre within FFRP, most likely due to photo-oxidation caused by UV irradiation rather than hydrolysis from wet-dry cycling. Notably, the epoxy coating exhibits high UV transmittance. Boumedienne and Maaroufi [88] reported approximately 98 % UV transmittance for an epoxy film with a thickness of 2600 nm. Based on the Beer-Lambert Law [89], it is estimated that the epoxy coating in this study, with a thickness of 1–2 mm, has a UV transmittance exceeding 90 %. On the

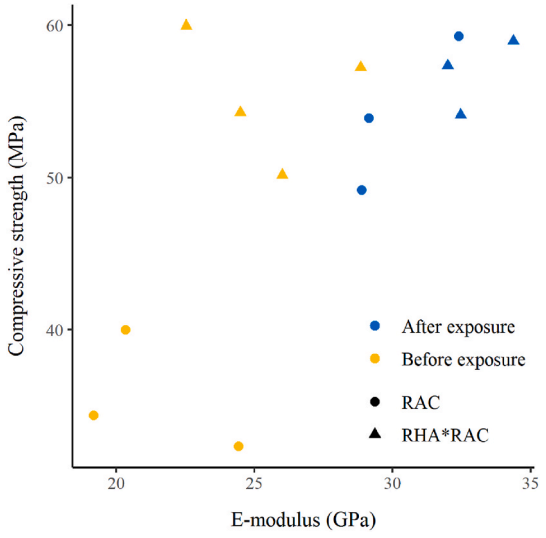

Fig. 15. Compressive properties of RAC and RHA*RAC cylinders before and after exposure.

other hand, hydrolysis of cellulose is less likely to occur in the wet-dry condition in this study, as it normally needs facilitation by acid, alkaline or enzyme. Huang et al. [22] found no cellulose degradation in flax fibre extracted from the reinforced polymer even under hygrothermal condition (50 °C, 95 % relative humidity). The wet-dry cycling primarily compromised the structural integrity of FFRP, as demonstrated and explained in Section 3.3.1. This resulted in not only debonding between the epoxy and flax yarn but also accelerated photo-degradation and compound leaching in the flax fibre, ultimately leading to a loss of mechanical capacity in the FFRP. On the contrary, cellulose degradation in the flax fibre within FFRP caused by UV irradiation did not significantly reduce the tensile properties of the FFRP, implying that the wet-dry cycling poses a greater threat to FFRP compared to UV light. In addition, the changes in the chemical composition of the flax fibre within FFRP, as well as the tensile properties of FFRP, were not as pronounced as those observed in the flax yarn. This suggests that the epoxy coating provided protection for the flax yarn against weathering exposure.

3.4. RAC

3.4.1. Changes in compressive properties and chemical composition

Fig. 15 presents the compressive strength and E-modulus of RAC and RHA*RAC cylinders before and after the exposure. A two-way analysis of variance (ANOVA) was performed on both properties, with concrete type and weathering exposure considered as the two main factors. The analysis revealed that, for compressive strength, both concrete type and exposure were significant factors (p-value = 0.0008 and 0.0024, respectively) along with their interaction (p-value = 0.0043). The subsequent Tukey's HSD test indicated that RAC experienced a significant increase in compressive strength after exposure compared to its original strength (adjusted p-value = 0.0015), whereas RHA*RAC showed no significant change (adjusted p-value = 0.9677). Meanwhile, the difference in compressive strength between RAC and RHA*RAC shifted from significant before exposure (adjusted p-value = 0.0006) to non-significant after exposure (adjusted p-value = 0.8498). In terms of E-modulus, both concrete type and exposure were significant factors (p-value = 0.0231 and < 0.0001, respectively), while their interaction was not significant. The following Tukey's HSD test indicated a significant increase in the E-modulus of RAC after exposure compared to its original E-modulus (adjusted p-value = 0.0007), as well as in the E-modulus of RHA*RAC (adjusted p-value = 0.0061). The E-modulus between RAC and RHA*RAC did not differ significantly either before or after exposure (both adjusted p-values >0.1).

Generally, the compressive strength and E-modulus of RAC were significantly lower than those of RHA*RAC before exposure. However, after exposure, both properties of RAC improved substantially, leading to non-significant differences when compared to RHA*RAC. This aligns with our previous study [37], which reported that replacing 10 % of cement with RHA in RAC enhanced the compressive strength and E-modulus at 28 days compared to RAC without RHA. Additionally, the compressive strength of RAC continued to increase significantly after 91 days of storage under room conditions compared to its 28-day strength [37]. Although prolonged wet-dry cycling and UV irradiation can potentially cause surface degradation of concrete—and wet-dry cycling may lead to mechanical degradation through repeated swelling and shrinkage, leaching of soluble compounds, and associated sulfate, chloride, or other salt attacks—the exposure conditions in this study were relatively moderate and of short duration. Therefore, it is unlikely that significant mechanical degradation of the concrete occurred under these conditions. In this case, the compressive properties of the concrete were primarily governed by its hydration process, which tended to result in an increase in compressive strength and E-modulus. Many studies reported an increase in compressive strength or E-modulus of cement-based materials under wet-dry cycling [90,91], UV irradiation [24] and real outdoor condition for one year [92]. Regarding the changes in compressive properties of RHA*RAC, no significant increase in the strength was observed after exposure. Given that the addition of RHA had already shown a significant effect on compressive strength prior to exposure, it is suspected that the filling effect of RHA primarily contributed to the

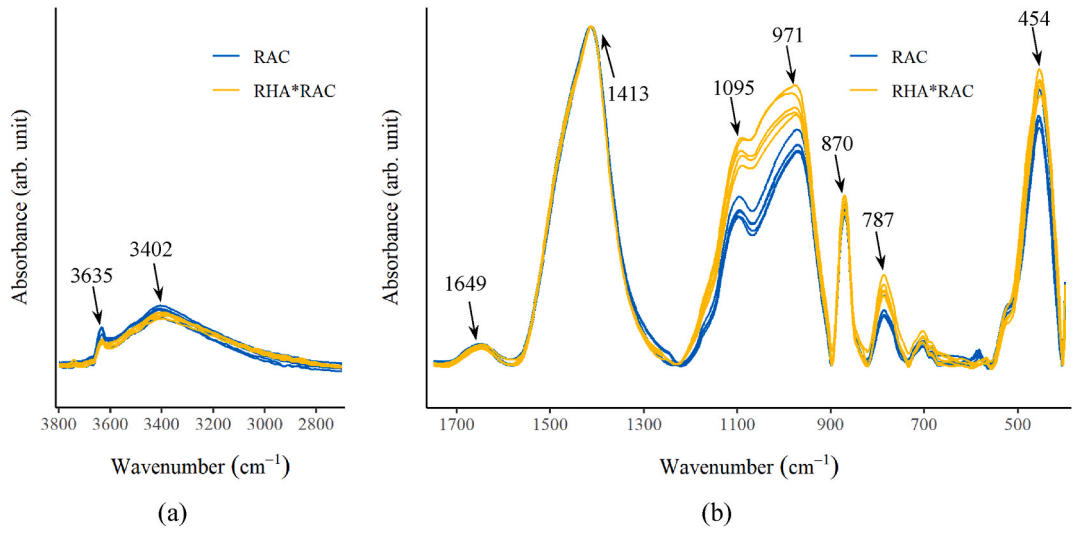

Fig. 16. Normalised FTIR spectra of the binder from RAC and RHA*RAC after exposure: (a) 3800–2700 cm^{-1} and (b) 1750–400 cm^{-1}.

improved compressive strength of RAC. This is because the pozzolanic reaction of RHA occurs over a longer timescale compared to the cement hydration process. This is further explained in the subsequent paragraphs by examining the changes in their chemical composition.

The FTIR spectra for binder extracted from RAC and RHA*RAC after weathering exposure are illustrated in Fig. 16. The spectra were normalised based on the intensity of the vibration at 1413 cm^{-1}, which is attributed to calcium carbonate formed through concrete carbonation [93–95]. This decision was made based on a previous study [38], which found no significant differences in carbonation depth between RAC and RAC incorporating RHA with a 10 % replacement ratio after up to 28 days of exposure in a carbonation chamber with a CO_2 concentration of (70 ± 5)%. Table 7 shows the assignments of the corresponding vibrations, with the wavenumbers highlighted in red indicating significant differences in integrated intensity between RAC and RHA*RAC, as determined by *t*-test. It revealed that significant differences occurred at 3635, 1100–950, 787 and 454 cm^{-1} (all adjusted p-values <0.05). The notably lower $Ca(OH)_2$ content in the exposed RHA*RAC compared to the exposed RAC, as evidenced by the peak at 3635 cm^{-1}, is an expected outcome. This reduction is attributed to the pozzolanic reaction between the amorphous SiO_2 in RHA and the $Ca(OH)_2$, resulting in its consumption. The bands at 1100–950, 787 and 454 cm^{-1} are all assigned to Si-O vibrations. Among these, the broad bands in the region of 1100–950 cm^{-1} are associate to calcium silicate hydrate (C-S-H) [93,95], whereas the bands at 787 and 454 cm^{-1} are more likely related to quartz or other silicate phases [93,95,96]. As shown in Table 1, the RHA contained more than 90 % SiO_2, some of which existed in crystalline phase as indicated in the X-ray diffraction pattern (Fig. 3 (b)). Therefore, the significant differences observed at 787 and 454 cm^{-1} can be attributed to the crystalline SiO_2 present in RHA. Additionally, the amorphous SiO_2 in RHA contributed to increased formation of pozzolanic reaction products, such as C-S-H and other silicates, resulting in a considerable increase in the integrated intensity at 1100–950, 787 and 454 cm^{-1}.

Overall, compared to RAC, RHA*RAC contained a higher amount of C-S-H (and other silicate phases) and crystalline SiO_2, while having a lower amount of $Ca(OH)_2$. C-S-H is the primary binding phase in concrete, responsible for its strength. Although crystalline SiO_2 does not participate in the pozzolanic reaction, its small particle size (as shown in Fig. 3 (a)) allows it to fill the pores in the concrete, resulting in a denser microstructure. These are the main factors contributing to the higher compressive strength and E-modulus of RHA*RAC compared to RAC, although the differences in both properties are not statistically significant after exposure (both adjusted p-value >0.1). On the contrary, RHA*RAC exhibited a significantly higher compressive strength than that of RAC before exposure (adjusted p-value = 0.0006). This suggests that the filling effect of RHA played a primary role in improving the compressive strength of RAC, as the pozzolanic reaction of RHA takes place over a longer timescale compared to the hydration process of cement.

3.5. FFRP reinforced RAC

3.5.1. Changes in morphology

Upon being removed from the climate chamber, all FFRP-reinforced RAC samples exhibited visible cracks. Fig. 17 illustrates the general cracking pattern, with horizontal and longitudinal cracks forming on each side. Basically, the cracks developed along the reinforcement rods, suggesting that the cracks formed due to differential moisture expansion between the concrete and the FFRP reinforcement. Literature indicates that flax fibre reinforced epoxy composites can experience thickness swelling of up to 4 % at 100 % relative humidity [97], while the wet expansion of concrete can reach as high as 40 με [98]. Additionally, the curvature of the panel, visible in Fig. 17 (b), may also be attributed to the differential swelling between the RAC and the FFRP reinforcement. This discrepancy in expansion and contraction induces internal stresses, leading to overall deformation.

3.5.2. Changes in tensile properties and chemical composition of flax fibre

Fig. 18 illustrates the stress-strain responses of FFRP-RAC and FFRP-RHA*RAC subjected to uniaxial tensile loading both before and after the weathering exposure. The corresponding parameters including tensile strength, toughness (calculated as the area under the stress-strain curve) and ultimate strain are presented in Table 8. Two-way ANOVA followed by Tukey's HSD test was conducted on all parameters. It only revealed that the addition of RHA is a significant main factor for the tensile strength (p-value = 0.0341), and the post hoc analysis found no significant differences between any of the groups at the significance level of 0.05 for any parameter. One difference was found to be significant at a level of 0.1, specifically in the tensile strength between FFRP-RAC before exposure and FFRP-RHA*RAC after exposure (adjusted p-value = 0.0523). The statistical analysis indicates that the weathering exposure up to 30 weeks has no significant effect on the tensile properties of FFRP-RAC or FFRP-RHA*RAC. However, the addition of RHA in RAC shows potential for preserving the tensile load capacity of the FFRP reinforced RAC. Further details will be discussed in the following paragraph.

Flax fibres extracted from exposed FFRP-RAC and FFRP-RHA*RAC were analysed using FTIR and compared to the original fibres. Fig. 19 presents the normalised spectra across various regions, highlighting evident differences among the groups. The integrated intensity of vibrations was calculated, and the significance of differences between groups was assessed using ANOVA, followed by Tukey's HSD test. Significant differences at the $\alpha = 0.05$ level were observed in the regions of 3600–3000 cm^{-1}, 1730 cm^{-1} and 700 cm^{-1}, where the flax fibre from FFRP-RAC exhibited a significant decrease in integrated intensity compared to the original fibre (p-values = 0.0325, 0.0161 and 0.0002, respectively). The fibre from FFRP-RHA*RAC also showed a significantly reduced integrated intensity compared to the original fibre at 700 cm^{-1} (p-value = 0.0014). According to Table 4, these findings suggest that the flax fibre embedded in FFRP-RAC underwent significant degradation in hemicellulose and cellulose crystallinity after exposure. In contrast, the fibre from FFRP-RHA*RAC exhibited a more moderate level of degradation. Notably, at 1730 cm^{-1}, the integrated intensity for the fibre from FFRP-RAC is nearly zero, whereas the vibration for the fibre from FFRP-RHA*RAC remains relatively pronounced. Additionally, statistical analysis was not performed for the vibrations in the 1130–950 cm^{-1} region, as the peaks at 1051 cm^{-1}, 1000 cm^{-1},

Table 7
Assignments in the FTIR spectra for the binder from RAC and RHA*RAC.

Wavenumber (cm^{-1})	Assignment	Reference
~3635	ν(O-H) ($Ca(OH)_2$)	[93,94]
~3402	ν(O-H) (H_2O)	[93,94]
~1413, ~870	ν(C-O) (carbonate)	[93–95]
1100–950	ν(Si-O) (C-S-H)	[24,93,95]
~787	ν(Si-O) (quartz, silicates)	[93,94]
~454	δ(Si-O) (quartz, silicates) or Si-O deformation in C-S-H	[93,95,96]

(ν: stretching and δ: scissoring; the vibrations at the wavenumbers highlighted in red show significant differences in integrated intensity between RAC and RHA*RAC after exposure, as determined by a *t*-test at the $\alpha = 0.05$ significance level.).

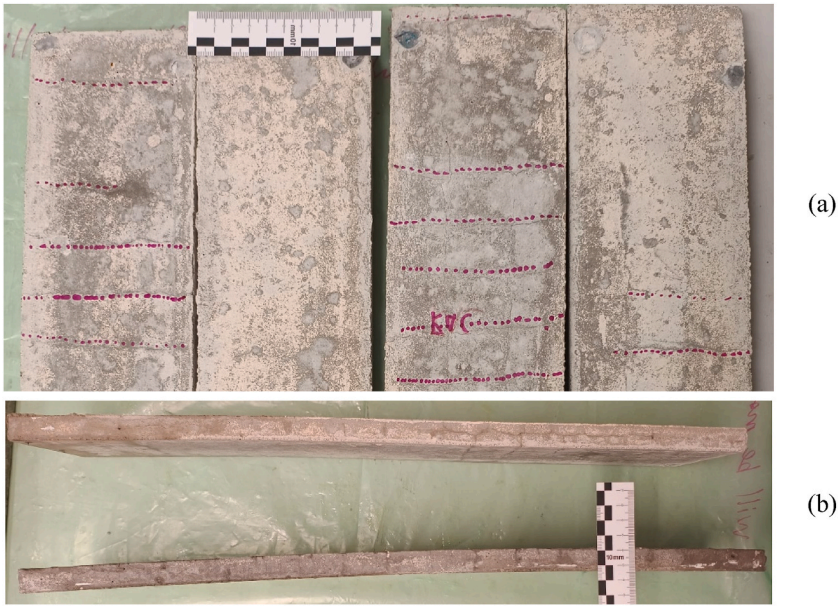

Fig. 17. Surface morphology of FFRP-RAC and FFRP-RHA*RAC after the weathering exposure: (a) front and (b) side view.

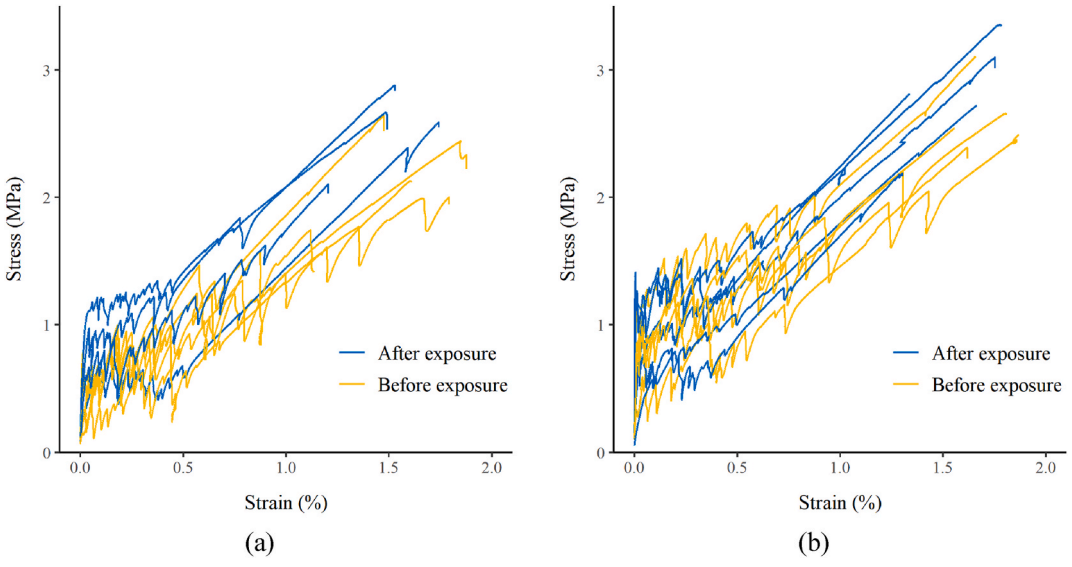

Fig. 18. Stress-strain responses under uniaxial tensile load before and after weathering exposure for: (a) FFRP-RAC and (b) FFRP-RHA*RAC.

Table 8
Tensile properties of two reinforced RAC groups before and after exposure (coefficients of variation are shown in parentheses).

		Tensile strength (MPa)	Toughness (J/mm^3)	Ultimate strain (%)
FFRP-RAC	Before exposure	2.19 (±16 %)	2.01 (±27 %)	1.58 (±19 %)
	After exposure	2.56 (±13 %)	2.28 (±24 %)	1.49 (±15 %)
FFRP-RHA*RAC	Before exposure	2.64 (±11 %)	2.79 (±18 %)	1.70 (±8 %)
	After exposure	2.83 (±15 %)	2.71 (±32 %)	1.56 (±15 %)

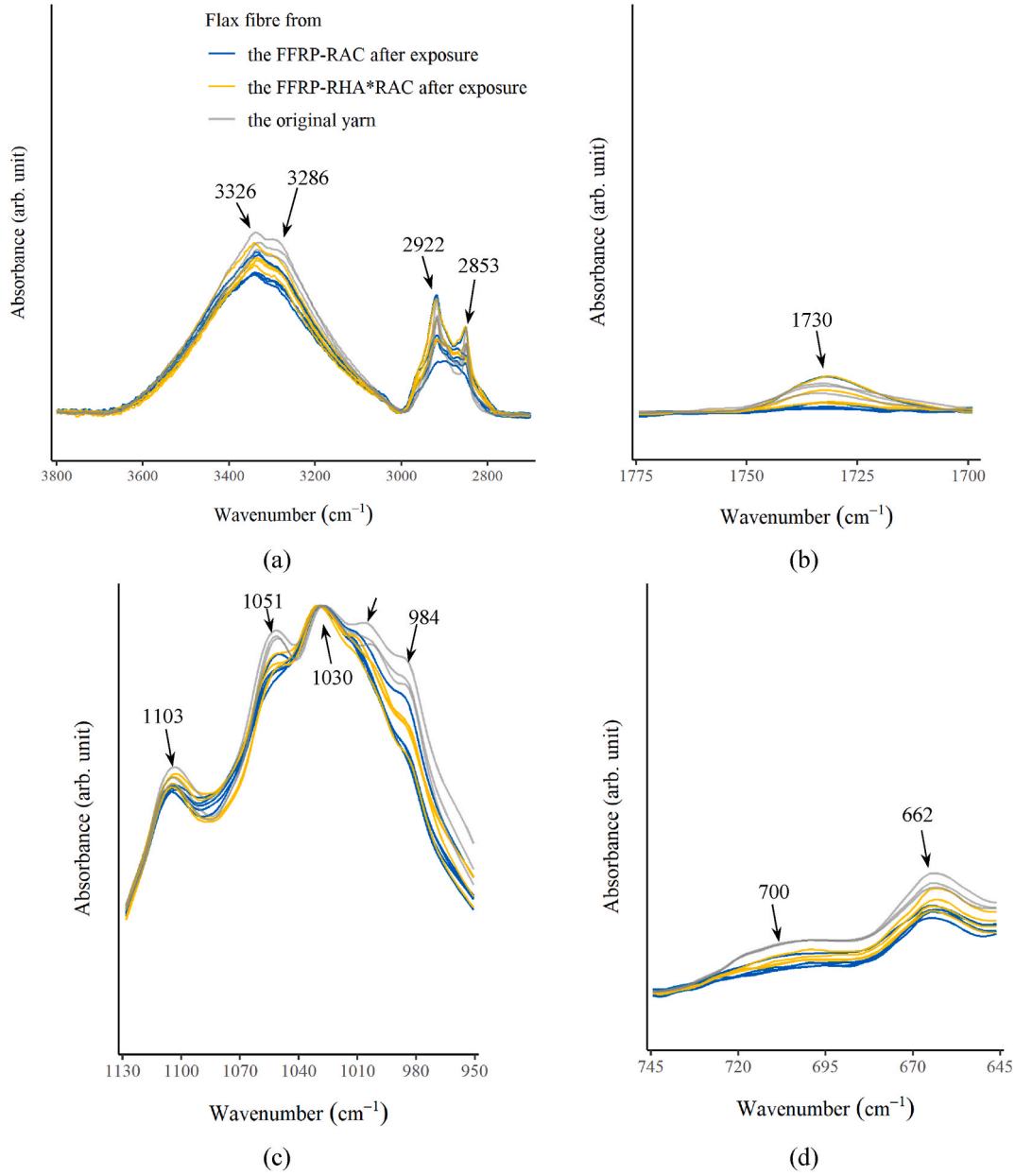

Fig. 19. Normalised FTIR spectra of flax fibres extracted from the exposed FFRP-RAC and FFRP-RHA*RAC compared to the original fibre: (a) 3800–2700 cm^{-1}, (b) 1775–1700 cm^{-1}, (c) 1130–950 cm^{-1} and (d) 745–645 cm^{-1}.

and 984 cm^{-1}—associated with cellulose or polysaccharides—were visibly diminished in the flax fibres from exposed FFRP-RAC and FFRP-RHA*RAC compared to the original fibre. Given the near-zero UV transmittance of concrete, the chemical degradation of flax fibres is primarily attributed to alkaline hydrolysis induced by the concrete environment. The FTIR results indicate that incorporating

RHA into the RAC helped mitigate flax fibre degradation, aligning with our previous findings [10]. The pozzolanic reaction of RHA consumes $Ca(OH)_2$, thereby reducing the alkalinity of the RAC. This lower alkalinity likely slows down alkaline hydrolysis of flax fibres, preserving the tensile load capacity of FFRP reinforced RAC as mentioned above.

In summary, the deterioration of FFRP reinforced RAC under weathering aging is primarily characterised by the alkaline degradation of the inner reinforcement material, mainly flax fibre, and the degradation of the interface between the FFRP and the RAC. Despite the absence of observable mechanical degradation in this study, the service life of FFRP reinforced RAC can be estimated based on its correlation with the duration of accelerated aging [99,100]:

$$\frac{A_0}{A_T} = 0.098 \times e^{(0.0558T)} \tag{1}$$

where A_0 represents the age in natural days; T indicates the conditioning temperature (°F); A_T denotes days of accelerated exposure at temperature T. Our precious study [10] examined the tensile properties of FFRP-RAC and FFRP-RHA*RAC under accelerated aging at 50 °C for 8, 19, and 30 weeks. According to Eq. (1), the corresponding natural durations are 13.5, 32.0 and 50.6 years. The tensile strength reduction of FFRP-RAC over these periods was 11 %, 16 % and 32 %, respectively, while for FFRP-RHA*RAC, it was 26 %, 6 % and 14 %, respectively. This suggests that incorporating RHA into the concrete can significantly enhance the service life of reinforced RAC with an estimated 86 % residual tensile strength after 50 years. A limitation of this study is that testing was performed only prior to exposure and after 30 weeks. Extended durations and multiple intermediate intervals should be explored in future work.

Unlike cellulosic textile reinforced concrete, moisture fluctuation is generally not a major concern for concrete reinforced with conventional synthetic textile materials, due to their low water absorption capacity. As a result, only a limited number of studies have investigated the aging behaviour of these systems under similar environmental conditions. For instance, a study by Mumenya et al. [101] reported a tensile strength retention of 128 % in polypropylene textile reinforced concrete after 14 months of wet-dry cycling, suggesting a possible continued hydration or post-curing effect. This is comparable to the 117 % tensile strength retention observed in the present study for flax textile-reinforced RAC. In contrast, a study by Le Trung Duc Pham et al. [102] on carbon textile reinforced concrete showed a tensile strength retention of 82 % after 25 wet-dry cycles conducted under harsher conditions (60 °C and Na_2SO_4 solution during the wetting phase). These more aggressive conditions likely contributed to the higher level of degradation observed. To enable reliable comparisons between different textile reinforcement strategies, direct experimental investigations under standardised conditions are essential.

3.5.3. Challenges in scaling up for real-world applications

Although eco-benefits of combining recycled aggregate, RHA and flax textile reinforcement are compelling, particularly in reusing construction & demolition wastes along with agricultural residuals and enabling lightweight, corrosion-resistant structures—the real-world scaling faces hurdles:

1) Regional limitation: Both RHA and flax fibre are highly regional in nature. RHA is predominantly available in areas with active rice production, such as South and Southeast Asia, as well as parts of Africa. Flax fibre suitable for technical applications is mainly produced in Western Europe. These geographical constraints limit the global competitiveness of these materials compared to more widely available supplementary cementitious materials, such as fly ash, silica fume, and metakaolin, and commonly used textile reinforcements, particularly those based on glass fibres. However, in other regions, context-specific alternatives may provide more practical and sustainable options. These include ashes derived from other agricultural residues (e.g., wheat husk ash, basil plant ash, peanut shell ash, and sunflower shell ash), as well as alternative cellulosic fibres (e.g., jute, hemp, or kenaf fibres).
2) Cost: As an agricultural by-product, RHA is relatively inexpensive, typically costing between €0.07 and €0.10 per kilogram in China [10]. Its price is generally higher than that of fly ash but lower than silica fume. Regarding reinforcement materials, flax mesh was purchased at €16.9/m^2 in Germany in 2020 for laboratory-scale quantities [10]. This price was approximately 3–4 times higher than that of glass mesh, yet about one-third the cost of carbon mesh.
3) Construction practices: Enhancing the pozzolanic activity of RHA typically requires pre-treatment processes such as controlled combustion and fine grinding, which can reduce its practicality in real-world applications and increase energy consumption. As for flax mesh reinforcement, a key challenge lies in maintaining dimensional stability during handling processes such as coating. This is primarily due to its lower rigidity compared to glass or carbon meshes. The issue becomes more pronounced as the mesh size increases, potentially affecting the precision and uniformity of application.
4) Long-term durability: Alkaline durability represents the primary challenge for flax textiles when embedded in concrete, particularly in comparison to alkaline-resistant glass and carbon textiles—a direct comparison among these materials should be conducted to quantify the differences. Notably, incorporating RHA into the cementitious matrix has shown promise: the strength loss of flax textile (with epoxy coating) reinforced RAC was reduced by 56 % after 30 weeks of accelerated alkaline exposure [10]. To further improve the durability of flax textile reinforced RAC structures, additional protective strategies should be developed. Moreover, long-term durability should be investigated under a wider range of environmental conditions, such as freeze-thaw cycles, cyclic loading, and varying thermal conditions.

4. Conclusions

This study investigates the impact of wet-dry cycling combined with UV irradiation on cementitious composites and their

individual components, including flax yarn, epoxy, FFRP, and RAC. The influence of these environmental factors on their mechanical properties and chemical compositions was evaluated. The key findings are summarised as follows:

1) The weathering exposure of flax yarns led to several detrimental phenomena, including compound leaching, fibrillation, and discoloration. Significant degradation in cellulose and hemicellulose, along with the formation of chromophoric compounds and microbial activity, was driven by cyclic water absorption and desorption in combination with photo-degradation. Correspondingly, the load capacity of the flax yarns decreased significantly, with only 7.4 % of the residual ultimate tensile load remaining. This reduction was not only due to fibre degradation but also because of damage to the structural integrity of the yarns.
2) The weathering exposure led to the breakdown of the amide groups and the aliphatic portions of the exposed epoxy samples. This degradation compromised the epoxy network, resulting in a significant reduction in its tensile strength, with a decrease of 20 %.
3) Within FFRP, the wet-dry cycling compromised its structural integrity, leading to interfacial debonding, whereas photo-oxidation resulted in notable cellulose degradation of flax fibre. However, no significant reduction in tensile strength or E-modulus of FFRP was observed.
4) RAC experienced a significant increase in both compressive strength and E-modulus after exposure, while for RHA*RAC, only the E-modulus increased significantly. Additionally, RHA*RAC showed a higher amount of C-S-H and crystalline SiO_2, while having a lower amount of $Ca(OH)_2$ compared to RAC after exposure. This observation confirm the pozzolanic reaction and filling effect of RHA in RAC.
5) Both FFRP-RAC and FFFRP-RHA*RAC did not show significant changes on tensile behaviour after exposure. The flax fibre embedded in FFRP-RAC underwent significant alkaline degradation in hemicellulose and cellulose crystallinity, whereas the fibre from FFRP-RHA*RAC exhibited a more moderate level of degradation. This indicate that incorporating RHA into the RAC helped mitigate flax fibre degradation, due to its pozzolanic reaction which consumed $Ca(OH)_2$, as discussed in point 4). This effect further helps preserve the tensile load capacity of FFRP-RHA*RAC.

In conclusion, the degradation mechanisms of FFRP reinforced RAC along with the individual components under wet-dry cycling combined with UV irradiation were studied. The findings demonstrate the beneficial role of RHA in mitigating flax fibre degradation and enhancing the durability of the composites. For future research and practical applications, it is essential to consider additional weathering factors such as freeze-thaw cycles, internal and external forces including creep, cyclic loading, and impact, along with aesthetic concerns like cracking and spalling.

Credit author statement

Wenzhuo Ma: Conceptualization, Writing, Original draft, Format analysis, Methodology, Design and conduction of Experiments. **Libo Yan:** Writing – review & editing, Supervision, Project administration, Methodology, Funding acquisition, Conceptualization.

Declaration of competing interest

The authors declare that they have no known competing financial interests or personal relationships that could have appeared to influence the work reported in this article.

Acknowledgements

This work is financially supported by Fachagentur Nachwachsende Rohstoffe e. V.v (FNR, Agency for Renewable Resources) founded by Bundesministerium für Ernährung und Landwirtschaft (BMEL, Federal Ministry of Food and Agriculture of Germany) (Grant No.: 22011617) and is also supported by Bundesministerium für Bildung und Forschung (BMBF, Federal Ministry of Education and Research of Germany) (Grant No.: 031B0914A). We wish to thank Xu Du for his assistance with the experimental work. We are also grateful to Moritz Micke-Camuz for providing technical support with the tensile testing of the flax yarns, and to Richard Deetz for overseeing the operation of the climate chamber. Furthermore, we extend our sincere appreciation to our project partners, Entsorgungstechnik Bavaria GmbH and Hunan University, for their provision of materials and support.

Data availability

Data will be made available on request.

References

[1] Entirely made of flax fibre. livMatS pavilion byICD/ITKE/INTCDC. https://www.metalocus.es/en/news/entirely-made-flax-fibre-livmats-pavilion-icditkeintcdc, 2021.
[2] D.F. van der Linden, The Application of Bio-based Composites in Load-Bearing Structures, Delft University of Technology, 2017. https://repository.tudelft.nl/islandora/object/uuid%3Ae6a03c90-de45-44e7-b2f6-74cf7b7d79d5?collection=education.
[3] A. Shahmirzaloo, M. Manconi, B. van den Hurk, B. Xu, R. Blok, P. Teuffel, Numerical and experimental validation of the static performance of a full-scale flax fiber-polyester composite bridge model to support the design of an innovative footbridge, Eng. Struct. 291 (2023) 116461, https://doi.org/10.1016/j.engstruct.2023.116461.

[4] R.S. Aouf, Smart circular bridge built with flax completes in the Netherlands. https://www.dezeen.com/2022/05/05/smart-circular-bridge-flax-completed-the-netherlands-architecture/, 2022.
[5] L. Yan, N. Chouw, K. Jayaraman, Flax fibre and its composites - a review, Composites, Part B 56 (2014) 296–317, https://doi.org/10.1016/j.compositesb.2013.08.014.
[6] J. Page, F. Khadraoui, M. Gomina, M. Boutouil, Enhancement of the long-term mechanical performance of flax fiber-reinforced cementitious composites by using alternative binders, J. Build. Eng. 40 (2021) 1–31, https://doi.org/10.1016/j.jobe.2021.102323.
[7] G. Ferrara, M. Pepe, E. Martinelli, R.D. Tolêdo Filho, Tensile behavior of flax textile reinforced lime-mortar: influence of reinforcement amount and textile impregnation, Cem. Concr. Compos. 119 (2021), https://doi.org/10.1016/j.cemconcomp.2021.103984.
[8] N. Trochoutsou, M. Di Benedetti, K. Pilakoutas, M. Guadagnini, Mechanical characterisation of flax and jute textile-reinforced mortars, Constr. Build. Mater. 271 (2021) 121564, https://doi.org/10.1016/j.conbuildmat.2020.121564.
[9] W. Ma, L. Yan, B. Kasal, Bond and tensile properties of flax textile reinforced recycled aggregate concrete: strategies for interfacial enhancement and corresponding mechanisms, Case Stud. Constr. Mater. 21 (2024) e04006, https://doi.org/10.1016/j.cscm.2024.e04006.
[10] W. Ma, L. Yan, R. Klingner, Enhancing long-term alkaline durability of epoxy-coated flax textile for internal concrete reinforcement: surface modification & matrix integration with rice husk ash, Constr. Build. Mater. 477 (2025) 141080, https://doi.org/10.1016/j.conbuildmat.2025.141080.
[11] W. Ma, L. Yan, B. Kasal, Intensive exploration: the application potential of flax fibre/textiles as reinforcement in cementitious composites, J. Clean. Prod. 507 (2025) 145457, https://doi.org/10.1016/j.jclepro.2025.145457.
[12] C. Schätzke, H.N. Schneider, Textile-reinforced concrete, in: M. Peck (Ed.), Concr. Des. Constr. Examples, Birkhäuser, München, 2006, pp. 32–37, https://doi.org/10.11129/detail.9783034614740.32.
[13] PwC – sustainable performance and strategy, life cycle assessment of CFGF – Continuous filament glass fibre products. https://doi.org/10.1111/fcre.12690, 2023.
[14] G. Wernet, C. Bauer, B. Steubing, J. Reinhard, E. Moreno-Ruiz, B. Weidema, The ecoinvent database version 3 (part I): overview and methodology, Int. J. Life Cycle Assess. 21 (2016) 1218–1230, https://doi.org/10.1007/s11367-016-1087-8.
[15] Y. Deng, Life Cycle Assessment of Biobased fibre-reinforced Polymer Composites, KU Leuven, 2014, https://doi.org/10.1142/9789814566469_0063.
[16] K. Kawajiri, K. Sakamoto, Environmental impact of carbon fibers fabricated by an innovative manufacturing process on life cycle greenhouse gas emissions, Sustain. Mater. Technol. 31 (2022) e00365, https://doi.org/10.1016/j.susmat.2021.e00365.
[17] N. de Beus, M. Carus, M. Barth, Carbon footprint and sustainability of different natural fibres for biocomposites and insulation material, carbon footpr, Nat. Fibres. (2019) 4–45. www.nova-institut.eu.
[18] P. Saha, S. Manna, D. Roy, M.C. Kim, S. Chowdhury, S. De, R. Sen, B. Adhikari, J.K. Kim, Effect of photodegradation of lignocellulosic fibers transesterified with vegetable oil, Fibers Polym. 15 (2014) 2345–2354, https://doi.org/10.1007/s12221-014-2345-7.
[19] L.M. do Amaral, C. de S. Rodrigues, F.S.J. Poggiali, Hornification on vegetable fibers to improve fiber-cement composites: a critical review, J. Build. Eng. 48 (2022), https://doi.org/10.1016/j.jobe.2021.103947.
[20] B. Xu, B. van den Hurk, T. Liu, R. Blok, P. Teuffel, Effect of UV-water weathering on the mechanical properties of flax-fiber-reinforced polymer composites, Polym. Compos. 45 (2024) 4266–4280, https://doi.org/10.1002/pc.28057.
[21] C. Wu, B.C. Meng, L. ho Tam, L. He, Yellowing mechanisms of epoxy and vinyl ester resins under thermal, UV and natural aging conditions and protection methods, Polym. Test. 114 (2022), https://doi.org/10.1016/j.polymertesting.2022.107708.
[22] S. Huang, L. Yan, B. Kasal, Y. Wei, Moisture diffusion and tensile properties of epoxy-based and polyurethane-based flax-glass hybrid FRP under hygrothermal and weathering environments, Composites, Part B 267 (2023) 111049, https://doi.org/10.1016/j.compositesb.2023.111049.
[23] I. Luhar, S. Luhar, P. Savva, A. Theodosiou, M.F. Petrou, D. Nicolaides, Light transmitting concrete: a review, Buildings 11 (2021) 1–18, https://doi.org/10.3390/buildings11100480.
[24] H. Wang, G. Long, Y. Xie, X. Zeng, K. Ma, R. Dong, Z. Tang, Q. Xiao, Effects of intense ultraviolet irradiation on drying shrinkage and microstructural characteristics of cement mortar, Constr. Build. Mater. 347 (2022) 128513, https://doi.org/10.1016/j.conbuildmat.2022.128513.
[25] H. Li, Z. Shui, Z. Wang, X. Xiao, Effects of UV radiation on the carbonation of cement-based materials with supplementary cementitious materials, Coatings 13 (2023), https://doi.org/10.3390/coatings13060994.
[26] B.J. Mohr, H. Nanko, K.E. Kurtis, Durability of kraft pulp fiber-cement composites to wet/dry cycling, Cem. Concr. Compos. 27 (2005) 435–448, https://doi.org/10.1016/j.cemconcomp.2004.07.006.
[27] B.J. Mohr, J.J. Biernacki, K.E. Kurtis, Microstructural and chemical effects of wet/dry cycling on pulp fiber-cement composites, Cement Concr. Res. 36 (2006) 1240–1251, https://doi.org/10.1016/j.cemconres.2006.03.020.
[28] C. Yaremko, Durability of Flax Fibre Reinforced Concrete, University of Saskatchewan, 2012.
[29] B. Poletanović, I. Merta, A. Šajna, A.M. Pranjić, A. Mladenović, Comparision of physical and mechanical properties of cementitious mortars reinforced with natural and synthetic fibres prior and after wet/dry cycles, in: 3rd Int. Conf. Bio-based Build. Mater., 2019, pp. 433–437. Belfast, UK.
[30] R. Toledo Filho, K. Scrivener, G.L. England, K. Ghavami, Durability of alkali-sensitive sisal and coconut fibres in cement mortar composites, Cem. Concr. Compos. 22 (2000) 127–143.
[31] G. Ferrara, B. Coppola, L. Di Maio, L. Incarnato, E. Martinelli, Tensile strength of flax fabrics to be used as reinforcement in cement-based composites: experimental tests under different environmental exposures, Composites, Part B 168 (2019) 511–523, https://doi.org/10.1016/j.compositesb.2019.03.062.
[32] P. Sadrolodabaee, J. Claramunt, M. Ardanuy, A. de la Fuente, Effect of accelerated aging and silica fume addition on the mechanical and microstructural properties of hybrid textile waste-flax fabric-reinforced cement composites, Cem. Concr. Compos. 135 (2023) 104829, https://doi.org/10.1016/j.cemconcomp.2022.104829.
[33] Ltd Bcomp, Product Data Sheet Powerribs, 2016.
[34] Gurit (UK) Ltd, Ampreg 31 Resin Safety Data Sheet, 2024. Newport, UK.
[35] Gurit Services AG, Ampreg^{tm} 31 Full General Datasheet, 2022.
[36] DIN EN 1097-6 Tests for Mechanical and Physical Properties of Aggregates - Part 6: Determination of Particle Density and Water Absorption, 2022.
[37] W. Ma, Y. Wang, L. Huang, L. Yan, B. Kasal, Natural and recycled aggregate concrete containing rice husk ash as replacement of cement : mechanical properties , microstructure , strength model and statistical analysis, J. Build. Eng. 66 (2023) 105917, https://doi.org/10.1016/j.jobe.2023.105917.
[38] W. Ma, B. Lv, Y. Wang, L. Huang, L. Yan, B. Kasal, Freeze-thaw , chloride penetration and carbonation resistance of natural and recycled aggregate concrete containing rice husk ash as replacement of cement, J. Build. Eng. 86 (2024) 108889, https://doi.org/10.1016/j.jobe.2024.108889.
[39] W. Ma, Y. Wang, L. Huang, L. Yan, B. Kasal, Optimisation and prediction of compressive properties for concrete containing recycled aggregates and rice husk ash using response surface methodology (RSM), Ce/Papers (2023) 1009–1014, https://doi.org/10.1002/cepa.2872.
[40] W. Ma, T. Kolb, N. Rüther, P. Meinlschmidt, H. Chen, L. Yan, Physical , mechanical , thermal and fire behaviour of recycled aggregate concrete block wall system with rice husk insulation, Energy Build. 320 (2024) 114560, https://doi.org/10.1016/j.enbuild.2024.114560.
[41] V.W.Y. Tam, C.M. Tam, Diversifying two-stage mixing approach (TSMA) for recycled aggregate concrete: TSMAs and TSMAsc, Constr. Build. Mater. 22 (2008) 2068–2077, https://doi.org/10.1016/j.conbuildmat.2007.07.024.
[42] ASTM Committee G03, ASTM G154-16 standard practice for operating fluorescent ultraviolet (UV) lamp apparatus for exposure of nonmetallic materials. https://doi.org/10.1520/G0154-16.2, 2016.
[43] DIN EN ISO 2062 Textiles - Yarns from Packages - Determination of single-end Breaking Force and Elongation at Break Using Constant Rate of Extension (CRE) Tester, 2010.
[44] T. Kolb, P. Meinlschmidt, N. Rüther, J. Winkelmann, M. Micke-Camuz, Verbesserte Ressourceneffizienz Nachwachsender Rohstoffe Durch Die Verwendung Von Land- Und Forstwirtschaftsabfällen Sowie Bau- Und Abbruchabfällen Für Eine Nachhaltige Gebäudewelt – Rematbuilt, 2024. Braunschweig.
[45] BSI committee, ISO 10406-1 fibre-reinforced Polymer (FRP) Reinforcement of Concrete - Test Methods Part 1: FRP Bars and Grids, 2013. London, UK.
[46] EN ISO 527-1 Plastics - Determination of Tensile Properties - Part 1: General Principles, 2019.

[47] RILEM Technical Committee 232-TDT (Wolfgang Brameshuber), TC-TDT, W. Brameshuber, M. Hinzen, A. Dubey, A. Peled, B. Mobasher, A. Bentur, C. Aldea, F. Silva, J. Hegger, T. Gries, J. Wastiels, K. Malaga, C. Papanicolaou, L. Taerwe, M. Curbach, V. Mechtcherine, A. Naaman, J. Orlowsky, P. Hamelin, H. W. Reinhardt, S. Shah, R. Toledo, T. Triantafillou, A. Si Larbi, D. Garcia, L. Garmendia, S. Gopinath, F. Jesse, Recommendation of RILEM TC 232-TDT: test methods and design of textile reinforced concrete: uniaxial tensile test: test method to determine the load bearing behavior of tensile specimens made of textile reinforced concrete, Mater. Struct. 49 (2016) 4923–4927, https://doi.org/10.1617/s11527-016-0839-z.
[48] DIN EN 12390-13, Testing Hardened Concrete - Part 13: Determination of Secant Modulus of Elasticity in Compression, 2021.
[49] B.H. Rafidison, H. Ramasawmy, J. Chummun, F.B.V. Florens, Using infrared spectrum analyses to predict tensile strength of fibres in a group of closely related plant species: case of Mascarenes Pandanus spp, SN Appl. Sci. 2 (2020) 1–13, https://doi.org/10.1007/s42452-020-03667-1.
[50] Y. Horikawa, S. Hirano, A. Mihashi, Y. Kobayashi, S. Zhai, J. Sugiyama, Prediction of lignin contents from infrared spectroscopy: chemical digestion and Lignin/Biomass ratios of Cryptomeria japonica, Appl. Biochem. Biotechnol. 188 (2019) 1066–1076, https://doi.org/10.1007/s12010-019-02965-8.
[51] R. Bahrami, R. Bagheri, C. Dai, Influence of fine structure on the variations of thermal and mechanical properties in flax fibers modified with different alkaline treatment conditions, J. Nat. Fibers 19 (2022) 5239–5257, https://doi.org/10.1080/15440478.2021.1875367.
[52] R. El Hage, R. Carvalho Martins, C. Brendlé, D. Lafon-Pham, R. Sonnier, Enhancing insight into photochemical weathering of flax and miscanthus: exploring diverse chemical compositions and composite materials, Molecules 29 (2024), https://doi.org/10.3390/molecules29163945.
[53] F.C. Fernandes, K. Kirwan, P.R. Wilson, S.R. Coles, Sustainable alternative composites using waste vegetable oil based resins, J. Polym. Environ. 27 (2019) 2464–2477, https://doi.org/10.1007/s10924-019-01534-8.
[54] Y. Jiang, M. Lawrence, A. Hussain, M. Ansell, P. Walker, Comparative moisture and heat sorption properties of fibre and shiv derived from hemp and flax, Cellulose 26 (2019) 823–843, https://doi.org/10.1007/s10570-018-2145-0.
[55] N. Abidi, L. Cabrales, C.H. Haigler, Changes in the cell wall and cellulose content of developing cotton fibers investigated by FTIR spectroscopy, Carbohydr. Polym. 100 (2014) 9–16, https://doi.org/10.1016/j.carbpol.2013.01.074.
[56] M. Schwanninger, J.C. Rodrigues, H. Pereira, B. Hinterstoisser, Effects of short-time vibratory ball milling on the shape of FT-IR spectra of wood and cellulose, Vib. Spectrosc. 36 (2004) 23–40, https://doi.org/10.1016/j.vibspec.2004.02.003.
[57] C. Margariti, The application of FTIR microspectroscopy in a non-invasive and non-destructive way to the study and conservation of mineralised excavated textiles, Herit. Sci. 7 (2019) 1–14, https://doi.org/10.1186/s40494-019-0304-8.
[58] P. Garside, P. Wyeth, Identification of cellulosic fibres by FTIR spectroscopy: thread and single fibre analysis by attenuated total reflectance, Stud. Conserv. 48 (2004) 269–275, https://doi.org/10.1179/sic.2003.48.4.269.
[59] L. Geminiani, F.P. Campione, C. Corti, M. Luraschi, S. Motella, S. Recchia, L. Rampazzi, Differentiating between natural and modified cellulosic fibres using ATR-FTIR spectroscopy, Heritage 5 (2022) 4114–4139, https://doi.org/10.3390/heritage5040213.
[60] M. Mir, L.D. Wilson, Flax fiber-chitosan biocomposites with tailored structure and switchable physicochemical properties, Carbohydr. Polym. Technol. Appl. 6 (2023) 100397, https://doi.org/10.1016/j.carpta.2023.100397.
[61] J. Kong, S. Yu, Fourier transform infrared spectroscopic analysis of protein secondary structures, Acta Biochim. Biophys. Sin. 39 (2007) 549–559, https://doi.org/10.1111/j.1745-7270.2007.00320.x.
[62] H.A. Krässig, Cellulose Structure, Accessiblity and Reactivity, second ed., Gordon and Breach Science Publishers, Philadelphia, 1993.
[63] M.L. Nelson, T. Mares, Accessibility and lateral order distribution of the cellulose in the developing cotton fiber, Textil. Res. J. 35 (1965) 592–603, https://doi.org/10.1177/004051756503500703.
[64] L. Salmén, E. Bergström, Cellulose structural arrangement in relation to spectral changes in tensile loading FTIR, Cellulose 16 (2009) 975–982, https://doi.org/10.1007/s10570-009-9331-z.
[65] A. Alonso-Simón, P. García-Angulo, H. Mélida, A. Encina, J.M. Álvarez, J.L. Acebes, The use of FTIR spectroscopy to monitor modifications in plant cell wall architecture caused by cellulose biosynthesis inhibitors, Plant Signal. Behav. 6 (2011) 1104–1110, https://doi.org/10.4161/psb.6.8.15793.
[66] M. Åkerholm, B. Hinterstoisser, L. Salmén, Characterization of the crystalline structure of cellulose using static and dynamic FT-IR spectroscopy, Carbohydr. Res. 339 (2004) 569–578, https://doi.org/10.1016/j.carres.2003.11.012.
[67] M. Jaouadi, S. M'sahli, F. Sakli, Optimization and characterization of pulp extracted from the Agave Americana L. fibers, Textil. Res. J. 79 (2009) 110–120, https://doi.org/10.1177/0040517508090781.
[68] M. Maache, A. Bezazi, S. Amroune, F. Scarpa, A. Dufresne, Characterization of a novel natural cellulosic fiber from Juncus effusus L, Carbohydr. Polym. 171 (2017) 163–172, https://doi.org/10.1016/j.carbpol.2017.04.096.
[69] S. Jana, W.H. Zhong, FTIR study of ageing epoxy resin reinforced by reactive graphitic nanofibers, J. Appl. Polym. Sci. 106 (2007) 3555–3563, https://doi.org/10.1002/app.26925.
[70] R. Darvishi Cheshmeh Soltani, A. Rezaee, M. Safari, A.R. Khataee, B. Karimi, Photocatalytic degradation of formaldehyde in aqueous solution using ZnO nanoparticles immobilized on glass plates, Desalination Water Treat. 53 (2015) 1613–1620, https://doi.org/10.1080/19443994.2013.855674.
[71] V. Soni, V. Goel, P. Singh, A. Garg, Abatement of formaldehyde with photocatalytic and catalytic oxidation: a review, Int. J. Chem. React. Eng. 19 (2021) 1–29, https://doi.org/10.1515/ijcre-2020-0003.
[72] W. Diao, H. Cai, L. Wang, X. Rao, Y. Zhang, Efficient photocatalytic degradation of gas-phase formaldehyde by Pt/TiO2 nanowires in a continuous flow reactor, ChemCatChem 12 (2020) 5420–5429, https://doi.org/10.1002/cctc.202000837.
[73] M.M. Amin, F. Teimouri, M. Sadani, M.A. Karami, Application of enhanced nZnO photocatalytic process with ultrasonic wave in formaldehyde degradation from aqueous solution, Desalination Water Treat. 57 (2016) 9455–9464, https://doi.org/10.1080/19443994.2015.1028453.
[74] D.L. Pavia, G.M. Lampman, G.S. Kriz, J.R. Vyvyan, Introduction to Spectroscopy, fifth ed., Cengage Learning, Stamford, USA, 2015 https://doi.org/10.1016/S1460-1567(00)80010-0.
[75] J. Parameswaranpillai, N. Hameed, J. Pionteck, E.M. Woo, Handbook of Epoxy Blends, Springer Cham, 2017, https://doi.org/10.1007/978-3-319-40043-3_3.
[76] C.A. Ramírez-Herrera, I. Cruz-Cruz, I.H. Jiménez-Cedeño, O. Martínez-Romero, A. Elías-Zúñiga, Influence of the epoxy resin process parameters on the mechanical properties of produced bidirectional [±45◦] carbon/epoxy woven composites, Polymers 13 (2021), https://doi.org/10.3390/polym13081273.
[77] A.E. Krauklis, A.T. Echtermeyer, Mechanism of yellowing: carbonyl formation during hygrothermal aging in a common amine epoxy, Polymers 10 (2018), https://doi.org/10.3390/polym10091017.
[78] X. Gu, W. Meeker, N. Tinh, J. Chin, Service life prediction of polymeric materials. https://doi.org/10.1007/978-0-387-84876-1, 2009.
[79] S. Tian, W. Ma, H. Li, C. Wang, Y. Xia, D. Lan, P. Zhou, D. Hu, Assessment of chemical degradation of epoxy resin binder used in the service of the Qin terracotta warriors, Sci. Rep. 14 (2024) 1–14, https://doi.org/10.1038/s41598-024-68442-3.
[80] W.U. Dewi, R. Sutrisna, H. Purnomo, M. Baiquni, Thermal decomposition of epoxy resin system used for filament winding, AIP Conf. Proc. 2941 (2023), https://doi.org/10.1063/5.0181753.
[81] N. Rajagopalan, C.E. Weinell, K. Dam-Johansen, S. Kiil, Degradation mechanisms of amine-cured epoxy novolac and bisphenol F resins under conditions of high pressures and high temperatures, Prog. Org. Coating 156 (2021), https://doi.org/10.1016/j.porgcoat.2021.106268.
[82] M. Sabu, E. Bementa, Y. Jaya Vinse Ruban, S. Ginil Mon, A novel analysis of the dielectric properties of hybrid epoxy composites, Adv. Compos. Hybrid Mater. 3 (2020) 325–335, https://doi.org/10.1007/s42114-020-00166-0.
[83] B. Wang, D. Li, G. Xian, C. Li, Effect of immersion in water or alkali solution on the structures and properties of epoxy resin, Polymers 13 (2021), https://doi.org/10.3390/polym13121902.
[84] M.G. González, J.C. Cabanelas, J. Baselga, Applications of FTIR on epoxy resins - identification, monitoring the curing process, phase separation and water uptake, Infrared Spectrosc. - Mater. Sci. Eng. Technol. 2 (2012), https://doi.org/10.5772/36323.
[85] B. Mailhot, S. Morlat-Thérias, M. Ouahioune, J.L. Gardette, Study of the degradation of an epoxy/amine resin, 1 photo- and thermo-chemical mechanisms, Macromol. Chem. Phys. 206 (2005) 575–584, https://doi.org/10.1002/macp.200400395.
[86] T. Scherzer, V. Strehmel, W. Tänzer, S. Wartewig, FTIR spectroscopy studies on epoxy networks, Phys. Polym. Networks. 205 (2007) 202–205, https://doi.org/10.1007/bfb0115501.

[87] A. Lavoratti, O. Bianchi, J.A. Cruz, Z. Al-Maqdasi, J. Varna, S.C. Amico, R. Joffe, Impact of water absorption on the creep performance of epoxy/microcrystalline cellulose composites, J. Appl. Polym. Sci. 141 (2024) 1–13, https://doi.org/10.1002/app.55365.
[88] N. Boumedienne, A. Maaroufi, Structural and opto-electronic properties of epoxy/silver nanocomposite films, Phys. B Condens. Matter 578 (2020), https://doi.org/10.1016/j.physb.2019.411853.
[89] J. Clark, The beer-lambert law, Chem. Libr (2015) 1–4. https://chem.libretexts.org/Bookshelves/Physical_and_Theoretical_Chemistry_Textbook_Maps/Supplemental_Modules_(Physical_and_Theoretical_Chemistry)/Spectroscopy/Electronic_Spectroscopy/Electronic_Spectroscopy_Basics/The_Beer-Lambert_Law.
[90] R. Kumar, N. Dev, S. Ram, M. Verma, Investigation of dry-wet cycles effect on the durability of modified rubberised concrete, Forces Mech. 10 (2023) 100168, https://doi.org/10.1016/j.finmec.2023.100168.
[91] J. Sainz-Aja, I. Carrascal, J. Polanco, A. Cimentada, C. Thomas, J. Brito, Aging of recycled aggregates mortars by drying-wetting cycles, Constr. Build. Mater. 307 (2021) 124934, https://doi.org/10.1016/j.conbuildmat.2021.124934.
[92] A.N. Giv, B. Asante, L. Yan, B. Kasal, Shear performance and durability of adhesively bonded spruce wood-concrete composite joints: effects of indoor and outdoor environmental conditions, mechanical load, and their coupled effect, Constr. Build. Mater. 436 (2024), https://doi.org/10.1016/j.conbuildmat.2024.136905.
[93] M. Horgnies, J.J. Chen, C. Bouillon, Overview about the use of fourier transform infrared spectroscopy to study cementitious materials, WIT Trans. Eng. Sci. 77 (2013) 251–262, https://doi.org/10.2495/MC130221.
[94] T. Hanzlicek, I. Perná, Z. Ertl, The influence of temperature and composition on modeled mortars, Int. J. Architect. Herit. 6 (2012) 359–372, https://doi.org/10.1080/15583058.2010.551702.
[95] S.A. Yaseen, G.A. Yiseen, Z. Li, Elucidation of calcite structure of calcium carbonate formation based on hydrated cement mixed with graphene oxide and reduced graphene oxide, ACS Omega 4 (2019) 10160–10170, https://doi.org/10.1021/acsomega.9b00042.
[96] M.O. Yusuf, Bond characterization in cementitious material binders using fourier-transform infrared spectroscopy, Appl. Sci. 13 (2023), https://doi.org/10.3390/app13053353.
[97] M.M. Lu, C.A. Fuentes, A.W. Van Vuure, Moisture sorption and swelling of flax fibre and flax fibre composites, Composites, Part B 231 (2022) 109538, https://doi.org/10.1016/j.compositesb.2021.109538.
[98] Y. Huang, B. Yuan, L. Xiao, Y. Liu, Studies on the wet expansion deformation of hydraulic concrete with fly ash under non-standard temperatures, Case Stud. Constr. Mater. 8 (2018) 392–400, https://doi.org/10.1016/j.cscm.2018.03.003.
[99] F. Micelli, M.A. Aiello, Residual tensile strength of dry and impregnated reinforcement fibres after exposure to alkaline environments, Composites, Part B 159 (2019) 490–501, https://doi.org/10.1016/j.compositesb.2017.03.005.
[100] K.L. Litherland, D.R. Oakley, B.A. Proctor, The use of accelerated aging procedures to predict the long term strength of GRF composites, Cement Concr. Res. 11 (1981) 455–466.
[101] S.W. Mumenya, R.B. Tait, M.G. Alexander, Mechanical behaviour of textile concrete under accelerated ageing conditions, Cem. Concr. Compos. 32 (2010) 580–588, https://doi.org/10.1016/j.cemconcomp.2010.07.007.
[102] L. Trung Duc Pham, U. Woo, K.K. Choi, H.J. Choi, Tensile characteristics of carbon textile-reinforced mortar incorporating short amorphous metallic and nylon fibers under designed environmental conditions, Constr. Build. Mater. 352 (2022), https://doi.org/10.1016/j.conbuildmat.2022.129059.